PHILIPS TECHNICAL REVIEW

Scanning-transmission electron microscope

Noise in semiconductor lasers

Metastable phases

PHILIPS

PHILIPS TECHNICAL REVIEW

Contents

The microprocessor-controlled CM12/STEM scanning-transmission electron microscope

U. Gross, F. J. M. Mescher and J. C. Tiemeijer
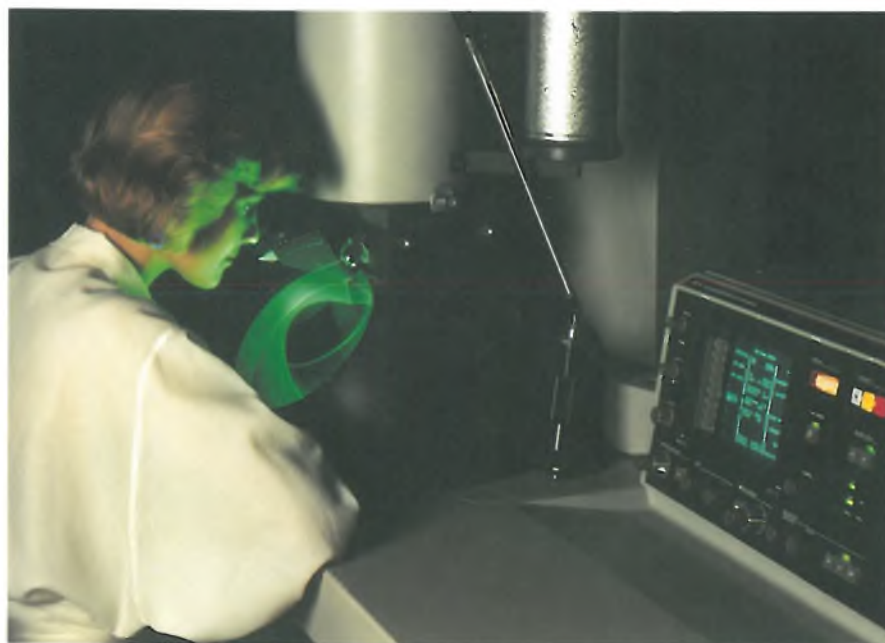
Continuous technological innovation in electron optics, mechanical engineering, electronics and vacuum engineering have earned Philips a leading position in the market for transmission electron microscopes. A recent invention is the Twin objective lens, which makes it possible to switch quickly from a transmission image to an image produced by scanning the specimen with the electron beam. In the latest microscope, the CM12/STEM scanning-transmission electron microscope, ease of operation has been considerably increased by the addition of microprocessor control. This microscope gives images that show that the microscope has a line resolution of 0.14 nm in the transmission mode and a point resolution of 1 nm in the scanning mode.

Introduction

The classical transmission electron microscope, as developed in the early thirties by Ernst Ruska and others, is comparable, in the geometry of the ray pattern, with a photographic enlarger or a slide projector. The extremely thin specimen is illuminated from

an electron source by means of one or more condenser lenses. The subsequent lenses produce a magnified image on a fluorescent screen, which converts the electron image into a visible image. The electron image can be recorded on photographic material.

The motivation for using electrons instead of visible light is of course to improve the resolution. Electrons at an energy of 120 kV are equivalent to electro-

Dr U. Gross, Ir F. J. M. Mescher and Ing. J. C. Tiemeijer are with the Philips Industrial and Electro-acoustic Systems Division, Eindhoven.

magnetic radiation at a wavelength λ of about 3.4×10^{-3} nm.

The wavelength λ is given by the relation

$$\lambda = \frac{h}{\sqrt{2em_0V^*}},$$

where h is Planck's constant, e the charge and m_0 the rest mass of the electron, and V^* a corrected value for the accelerating voltage V, taking account of the relativistic change of mass. V^* is given by the relation

$$V^* = V(1 + \frac{e}{2m_0c^2}V),$$

where c is the velocity of light. A useful expression, which does not take the relativistic change of mass into account and is valid for accelerating voltages lower than about 100 kV, is:

$$\lambda = \frac{1.23}{\sqrt{V}} \text{ nm},$$

where the accelerating voltage V is in volts.

The wavelength in an electron microscope is thus about 100000 times smaller than in an optical microscope. The resolution of an electron microscope, however, is not 100000 times better [1]. This is because the resolution is not merely proportional to the wavelength; it is also inversely proportional to the aperture angle of the objective lens. In an electron microscope the aperture angle has to be very much smaller than that of an optical microscope. The main reason for this is the need to minimize spherical aberration. The magnetic lenses that are combined to form the column of a modern electron microscope always have a positive spherical aberration, which means to say that the lenses are stronger for peripheral rays than for rays at the centre. Spherical aberration, unlike most other lens errors, cannot therefore be corrected.

It is perhaps interesting to illustrate the structure of a classical electron microscope by referring to a photograph and diagrams of the first microscope that Philips put on the market: the EM 100 of 1950; see *fig. 1* [2]. This microscope had one condenser lens and four image-forming lenses. These were a considerable improvement at the time, because the addition of a 'diffraction lens' made it possible to observe an ordinary image and an electron-diffraction pattern one after the other. This diffraction pattern related to a very small part of the specimen, selected by means of an SA diaphragm (SA for 'selected area'). The principle was due to Prof. J. B. le Poole and was for a long time the only way in which information about local crystal structures could be obtained in a transmission electron microscope [1].
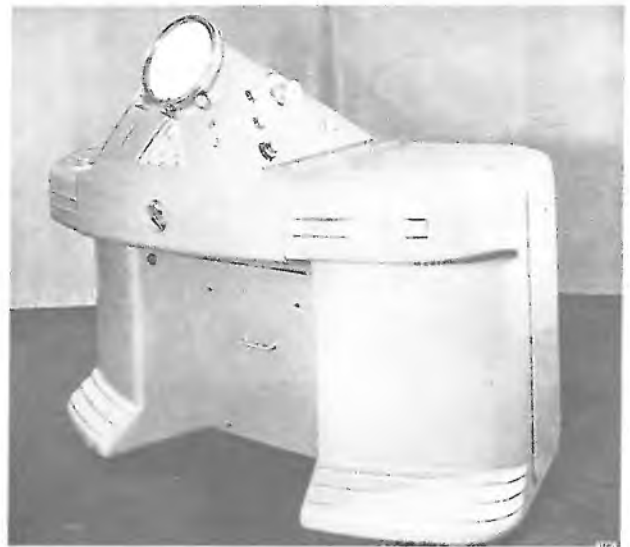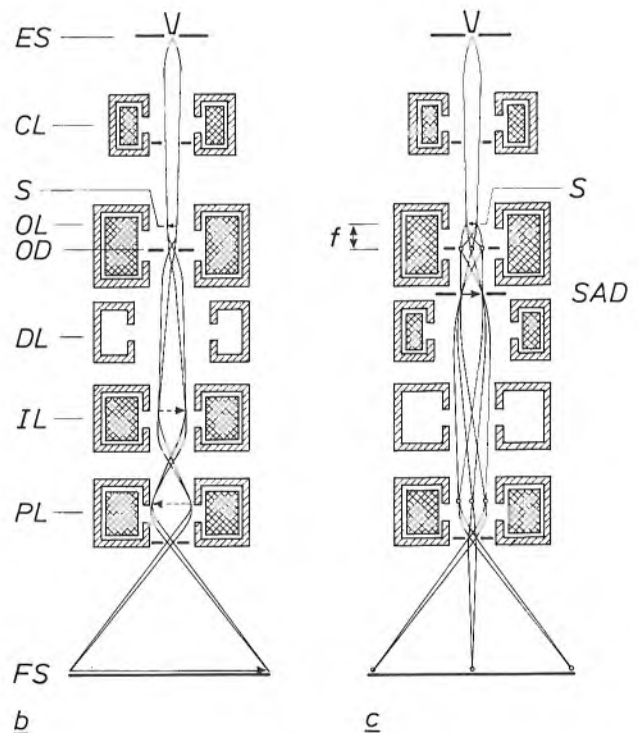
Fig. 1. *a*) The EM 100 transmission electron microscope, which Philips put on the market in 1950. (This microscope had a horizontal column to facilitate observation of the fluorescent screen.) *b*) The ray diagram for observing a highly magnified image of the specimen. *ES* electron source. *CL* condenser lens. *OL* objective lens. *DL* diffraction lens. *IL* intermediate lens. *PL* projector lens. *FS* fluorescent screen. The lenses with the cross-hatched coils are in operation. *S* specimen. *OD* objective diaphragm. *c*) The ray diagram for observing an electron-diffraction pattern. *SAD* selected-area diaphragm. *f* focal length of the objective.

Fig. 1*b* shows the important part played by the objective diaphragm *OD*, which is located at the back focal plane of the objective lens. It intercepts electrons that are scattered in the specimen, and is a useful aid for varying contrast in the image. Fig. 1*c* shows

that, with parallel illumination of the specimen, a diffraction pattern is formed at the back focal plane of the objective. To obtain an image of this diffraction pattern the objective diaphragm must be removed. This diaphragm does have to be used, however, for producing an ordinary image. If the aperture of the diaphragm coincides with the image of the electron source formed by the electrons transmitted through the specimen, not scattered in the specimen (fig. 1b), the image formed on the screen is called a bright-field image. This image, which is the one normally used, has contrasts different from those in a 'dark-field' image. A dark-field image is obtained by tilting the illuminating beam in such a way that the aperture of the objective diaphragm coincides with the image of the electron source formed by electrons that have been scattered over a defined angle in the specimen.

Philips transmission electron microscopes have undergone continuous improvement in the last 30 years [3]. While there have been a number of more gradual modifications and refinements, the emergence of another type of electron microscope, the scanning electron microscope, has considerably accelerated the evolution of transmission electron microscopes. Experience gained with scanning electron microscopes [4] — developed mainly for scanning the surface of large specimens with a narrow electron beam — and with electron microprobes [5] — developed primarily for wavelength-dispersive analysis of X-radiation from large specimens with a crystal spectrometer — has led to the realization that additional information could be obtained in a transmission electron microscope by scanning the specimen.

In the seventies this resulted in the development of a 'STEM' accessory unit for the Philips transmission electron microscope (STEM is an acronym for Scanning-Transmission Electron Microscope). With this electronic unit the electron beam can be made to 'write' a rectangular raster across the specimen. The electron gun of a cathode-ray tube in the STEM unit is controlled by a signal from a detector, and produces an image on its screen in which the contrast is obtained by techniques different from the conventional methods. Fig. 2 shows the detectors that are available for these techniques. The signals from the different detectors originate from:
• high-energy electrons back-scattered from the specimen (BSD),
• low-energy electrons produced by secondary emission in the specimen (SED),
• X-rays emitted by excited atoms in the specimen (EDX),
• non-scattered transmitted electrons (BFD),
• scattered transmitted electrons (DFD),

• transmitted electrons of specific, selected energy (EELS).

It should be noted that this evolution from a classical transmission electron microscope (TEM) to a scanning-transmission electron microscope (STEM) does not mean that the 'ordinary' scanning electron microscope (SEM) has become redundant. An SEM has its own specific range of applications, for the investigation of much larger and thicker specimens. Very often the SEM can also be used for wavelength-dispersive analysis of X-radiation, whereas a STEM
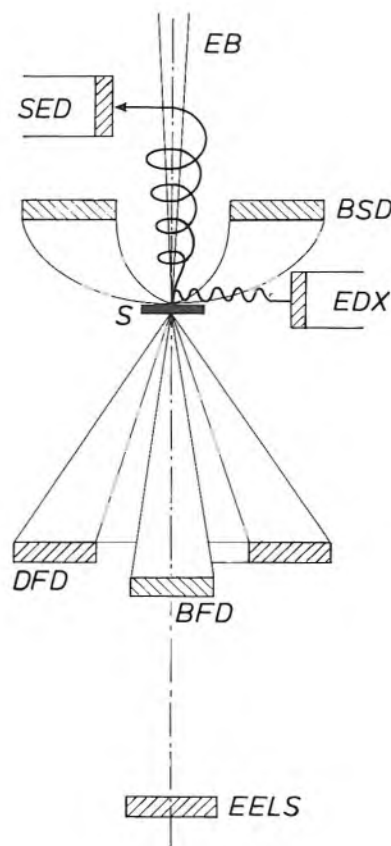
Fig. 2. Schematic representation of the detectors around the specimen and in the projection chamber. The detectors are mainly used when the instrument is used as a scanning-transmission electron microscope (STEM). EB electron beam. SED secondary-electron detector. BSD back-scattered electron detector. EDX detector for energy-dispersive X-ray analysis. BFD bright-field detector, for non-scattered transmitted electrons. DFD dark-field detector, for scattered transmitted electrons. EELS electron-energy-loss spectroscopy detector, for transmitted electrons sorted by energy; see also fig. 9.

[1] J. B. le Poole, A new electron microscope with continuously variable magnification, Philips Tech. Rev. 9, 33-45, 1947/48.
[2] A. C. van Dorsten, H. Nieuwdorp and A. Verhoeff, The Philips 100 kV electron microscope, Philips Tech. Rev. 12, 33-51, 1950/51.
[3] C. J. Rakels, J. C. Tiemeijer and K. W. Witteveen, The Philips electron microscope EM 300, Philips Tech. Rev. 29, 370-386, 1968.
[4] W. Kuypers and J. C. Tiemeijer, The Philips PSEM 500 scanning electron microscope, Philips Tech. Rev. 35, 153-165, 1975.
[5] M. Klerk, The electron microprobe, Philips Tech. Rev. 34, 370-374, 1974.

can only perform an energy-dispersive analysis with a solid-state detector. In scanning a specimen, however, a STEM will give a better resolution than that of most SEMs, since it has a finer beam, which is not broadened so much in the thin specimen.

The first Philips transmission microscopes of the EM 400 series appeared on the market in 1975. These microscopes have a column that facilitates the addition of a STEM accessory. The column has two condenser lenses and five image-forming lenses. The large number of lenses provided more facilities for eliminating chromatic magnification errors, radial distortion and image rotation. In addition, a cross-over point could be created for all the geometric ray patterns at a fixed position just beneath the final lens. It was then possible to use a diaphragm with an aperture of 200 μm cross-section, to separate the column from the projection chamber, where the fluorescent screen and the photographic material are located. In this arrangement an oil-free ion-getter pump can maintain a clean vacuum in the column and in the emission chamber, containing the electron source. This, and the use of

metal bellows instead of rubber rings, meant that a very clean environment could be created for the specimen and the filament. Consequently there is very little contamination of the specimen by hydrocarbons and the filament has a long life. Another advantage of these microscopes is that they no longer have to be mechanically aligned, since the alignment is done with correction coils.

In 1978 the Twin objective lens was introduced [6]. A microscope with this objective can easily be switched from a broad beam for normal images to a narrow beam for scanning images and analyses. Switching between broad beam and narrow beam does not change the heat flow in the objective, so that there is hardly any change in its dimensions. Nor is it necessary to change the polepieces. The objective has so much space between the polepieces that there is room for detectors and for a maximum specimen tilt through an angle of $\pm 60°$. Since the distance between the specimen and the X-ray detector is therefore small, more of the X-radiation emitted by the specimen can be intercepted and measured. The large tilt angle is useful for crystallographic electron-diffraction analyses.

The Twin objective is a modified immersion objective of the Riecke and Ruska type, with the specimen half-way between the polepieces. The specimen is located at the common focal plane of the two lenses formed by the magnetic field between the polepieces. Added to the immersion objective is a 'minilens', which acts as a third condenser lens. A special magnetic configuration allows the minilens to be switched off optically by simply reversing the current in the associated coil. This explains the high stability of the Twin objective. By making the mini-condenser lens optically inactive or active the minimum cross-section of the 'spot' at the specimen can be made either 1.5 nm or 0.04 μm. The smaller spot is called the 'nanoprobe' spot and the larger one the 'microprobe' spot.

With its Twin objective, a STEM unit and various detectors a Philips transmission-electron microscope can be used for a wide range of analyses. It can also produce transmission and scanning images of high resolution. *Fig. 3* shows the EM 420 microscope complete with all the accessory units for various purposes. Although the microscope is highly versatile and is virtually a complete laboratory in itself, its use requires a thorough knowledge of electron optics and analysis techniques. The complexity of an electron microsope with all these additional facilities is clear from the number of controls — 250 in all.

Recently Philips have introduced the scanning-transmission electron microscope type CM12/STEM,

Fig. 3. The EM 420 transmission electron microscope complete with all accessories. The Dewar vessel immediately to the right of the column contains liquid nitrogen for cooling the energy-dispersive X-ray detector (*EDX* in fig. 2); below this and to the right is the electronic unit for displaying the X-ray spectrum. On the extreme right is the STEM unit. This, like most other accessory units, is integrated into the latest electron microscope, CM12/STEM; see fig. 4.

b

Fig. 4. *a*) The CM12/STEM scanning-transmission electron microscope, which is much easier to operate than the microscope in fig. 3. On the left in the lower panel is the control screen for communication between user and the microprocessor — the heart of the instrument. The upper control panel contains two monitor screens, which display the STEM images. On the extreme right is the 'videoscope', an accessory that displays the brightness variation for one image line. *b*) Close-up of the control screen, with 'soft keys' on either side; the user uses these to communicate his requirements to the control software.

a

shown in the photograph of *fig. 4a*. In this instrument all the features of the EM 420 in fig. 3 are *integrated,* and all the electronic circuits are controlled by a microprocessor. This microprocessor guides the user to the various features available — a very useful facility. The microprocessor first offers the user, via the control screen (see fig. 4b), a choice of the modes he can work with, where a mode is a setting with a particular ray pattern. All the necessary operations are then carried out in an interactive dialogue with the user. The user requires less expertise in electron optics, and can now concentrate more closely on his investigations. In each mode the values of currents in the correction coils can remain stored in the microprocessor's memory. If the user wishes to depart from the programmed settings, he can adjust the lens currents to

suit his own requirements. Since there are no longer any fixed electrical connections between the controls and the electronics, there are far fewer manual controls. Consequently the CM12/STEM electron microscope is almost as easy to operate as the EM 100 in fig. 1, but it offers many more facilities and the resolution is incomparably better.

We shall now take a closer look at the electron-optical aspects of the instrument, dealing first with the Twin objective and then with the various modes. Then we shall touch briefly on the microprocessor control system. Finally, we shall demonstrate the features of the CM12/STEM with some micrographs of very dissimilar specimens.

[6]　The Twin lens is patented; the number of the patent in the United States is 4306149.

The electron optics

Fig. 5 shows a schematic cross-section of the column with emission chamber and projection chamber. The illumination system consists of the electron gun with filament and (electrostatic) Wehnelt lens, two condenser lenses, the minilens and the upper half of the objective lens. The last two lenses also act as a condenser lens and form part of the Twin objective,
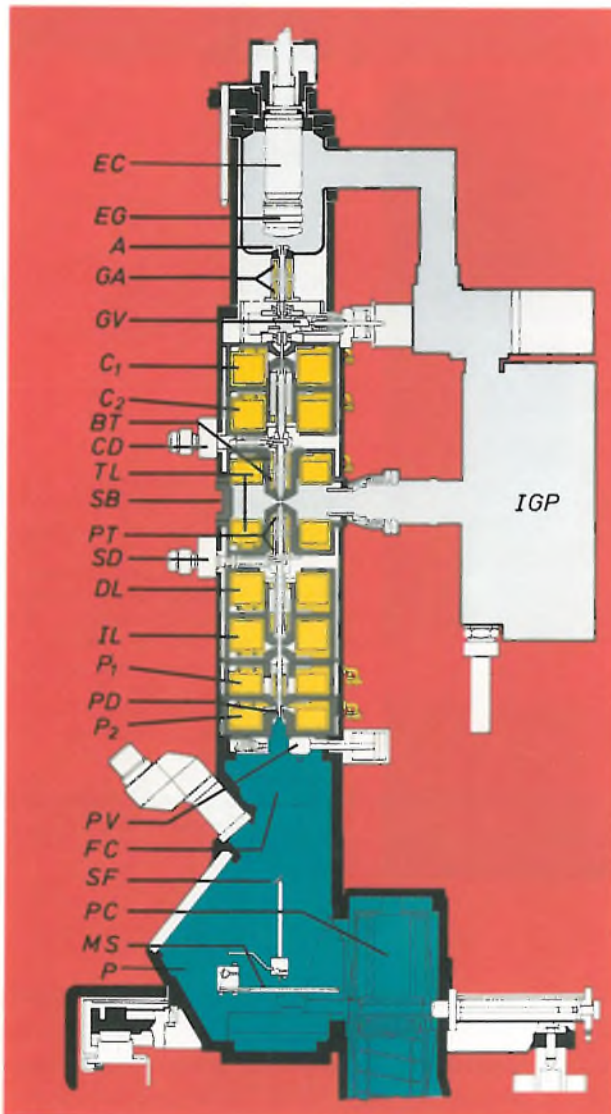

Fig. 5. Cross-section of the microscope column. *EC* emission chamber. *EG* electron gun. *A* anode. *GA* deflection coils for electron-gun alignment. *GV* valve for separately venting the emission chamber. C_1 first condenser lens. C_2 second condenser lens. *BT* beam-deflection coils above the specimen. *CD* condenser-diaphragm holder. *TL* Twin-objective lens. The mini-condenser lens is not shown (see fig. 7). *SB* block for accommodating the 'goniometer' (not shown); the goniometer permits the specimen in the specimen holder to be displaced. *PT* deflection coils below the specimen. *SD* SA diaphragm holder. *DL* diffraction lens. *IL* intermediate lens. P_1 first projector lens. *PD* partition diaphragm. P_2 second projector lens. *PV* valve for separately venting the projection chamber. *FC* film camera. *SF* fluorescent screen, for accurate focusing with a binocular magnifier. *PC* plate camera. *MS* fluorescent screen for observing the image through lead-glass windows in the projection chamber *P*, see also the title photograph. *IGP* ion-getter pump.

which we shall return to presently. The image-forming system consists of the lower half of the objective lens, the diffraction lens, the intermediate lens and two projector lenses.

At various positions in the column there are correction coils, which correct the beam for errors due to geometric imperfections and material inhomogeneities. The correction coils consist of:
• stigmator coils, for eliminating beam astigmatism, and
• deflection coils; these correct errors in deflection but their main function is to alter the direction of the beam so that it writes a rectangular raster across the specimen, for example.

The stigmator coils are oriented radially and arranged in sets of eight with an angle of 45° between them, as shown in *fig. 6a*. The deflection coils are combined in groups of four at 90° spacing. Two of these groups placed one above the other can produce a wide range of deflections in two perpendicular planes through the optical axis, as illustrated in fig. 6*b*, *c* and *d*. Two coils are shown from each group of four; the beam deflection is only shown in one plane through the optical axis. The correction coils free the user from the need for mechanical adjustment of the lenses.

At various positions in the column there are diaphragms that are adjustable in position and interchangeable, with a choice of four different sizes. These are:
• the condenser diaphragm, in the illumination system;
• the objective diaphragm, just beneath the specimen in the back focal plane of the lower half of the objective lens; and
• the SA diaphragm, in the image-forming system.
The column also contains fixed diaphragms, whose aperture cannot be changed. There is also a partition diaphragm (*PD* in fig. 5) of 200 μm cross-section, as mentioned earlier, which separates the vacuum in the column from that in the projection chamber. Water vapour from the photographic material and oil vapour from the diffusion pump and backing pump, which are connected to the projection chamber, are thus prevented from contaminating the specimen and reducing the life of the filament. The vacuum in the emission chamber and specimen chamber are maintained by a 'dry' ion-getter pump, i.e. one that requires no oil for its operation.

The specimen is placed in a specimen holder, which is slid through a vacuum lock into the specimen stage or 'goniometer'. The specimen can then be displaced in two directions at right angles to each other over an area of 2 mm by 2 mm and also tilted through a maximum angle of ± 60° about an axis in the plane
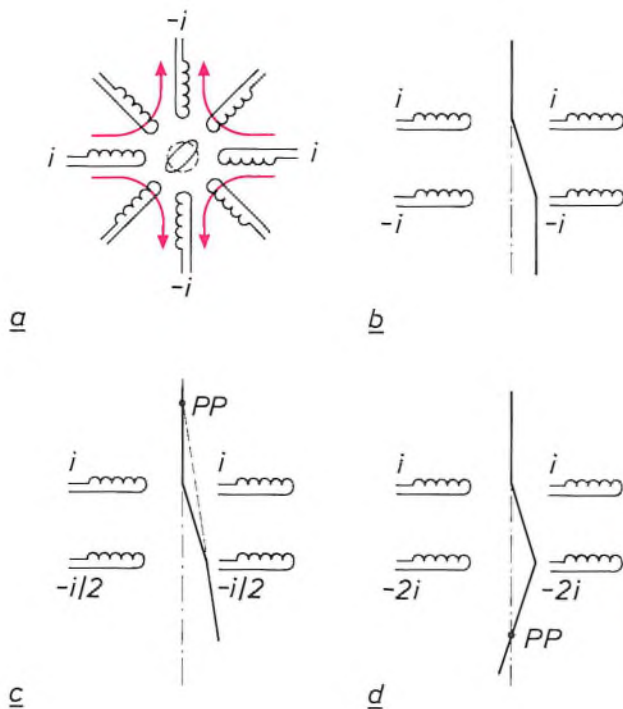
Fig. 6. The correction coils. *a*) A set of eight stigmator coils, used for correcting beam astigmatism. The diagram shows how an elliptical cross-section of the beam is changed into a circular cross-section by currents i and $-i$ in four of the eight coils. The magnetic lines of force are shown red. *b*) Deflection coils that not only correct errors in the beam direction but also cause the illuminating beam to describe a line across the specimen, as illustrated here schematically. (The deflection of the beam shown corresponds to a direction of the field and hence of the coils perpendicular to the plane of the drawing; the coils as shown are thus rotated through 90°; this also applies to *c* and *d*.) *c*) In this mode of energization the beam rotates about an imaginary pivot point *PP* above the coils. *d*) The same situation, but now with the pivot point below the coils. In certain modes, e.g. the dark-field mode with conical illumination, *PP* is in the specimen.

of the specimen. The special feature here is that this axis intersects the optical axis in every position of the specimen. This is referred to as a 'eucentric' movement of the specimen. The advantage is that the tilt axis always appears to go through the centre of the image on the user's screen. In addition to the standard specimen holder there are special specimen holders in which the specimen can be rotated, stretched, cooled or heated, and can always be tilted.

The Twin objective lens

In modern electron microscopes the specimen is not situated above the objective lens but inside it. The lens system is known as an immersion objective. In the symmetrical immersion objective proposed by Riecke and Ruska the specimen is situated exactly half-way between the polepieces [7]. Such a lens is a 'condenser objective' [8], with the part of the magnetic field above the specimen acting as a condenser lens and the part of the field below it as an image-forming lens. In an analogy with ordinary optics we can think

of a strong biconvex glass lens, which is cut in half perpendicular to the optical axis. The two identical halves are then moved away from each other through a distance of twice their focal length, and the specimen can then be considered to be located in the common focal plane between them.

The Twin objective lens is a symmetrical immersion objective to which a condenser lens, the minilens, has been added; see *fig. 7* [9]. The minilens is situated im-
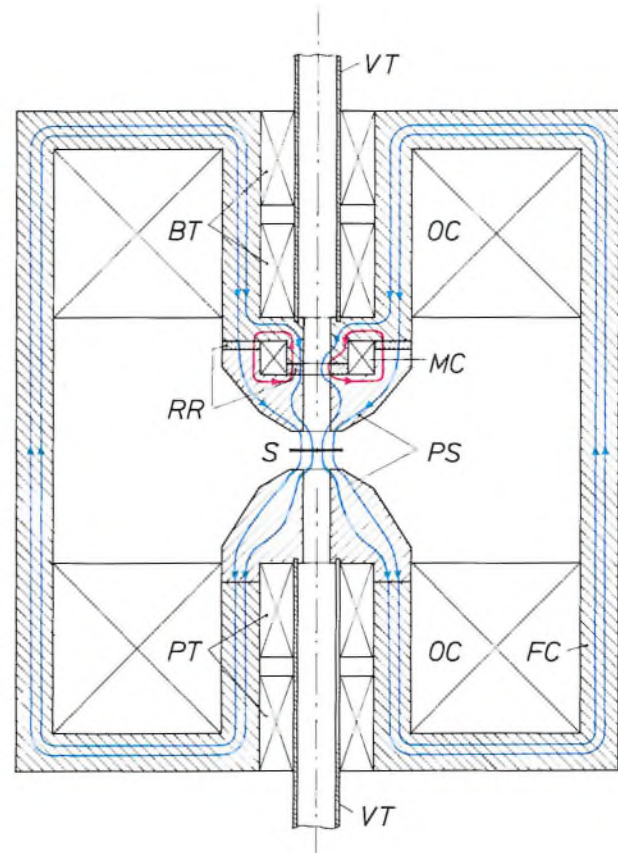
Fig. 7. The Twin objective lens [6]. *PS* polepieces. *FC* ferromagnetic core, including the coils *OC*. *BT* and *PT* deflection coils above and below the specimen *S*. *MC* mini-condenser coil. *RR* reluctances. *VT* stainless-steel tubes, enclosing the vacuum for the electron beam. The goniometer (not shown) is located between the coils *OC*; there is therefore another partition between the vacuum and these coils. In the left-hand half of the figure the minilens is not active; in the right-hand half it is. The blue magnetic lines of force are produced by a current in the coils *OC*. Because of their curvature, these lines of force form a positive lens both below and above the specimen; see also fig. 8. The red lines of force are the result of a current in the coil *MC*. In the right-hand half the red lines of force and the blue lines of force together form the mini-condenser lens, because of their curvature. In the left-hand half the current in *MC* is reversed, so that the red and blue lines of force counteract each other, causing the mini-condenser lens to become optically inactive here.

[7] W. D. Riecke and F. Ruska, A 100 kV transmission electron microscope with single-field condensor objective, Proc. Int. Cong. on Electron Microscopy Vol. 1, Kyoto 1966, pp. 19-20.
[8] J. R. A. Cleaver, The choice of polepiece shape and lens operating mode for magnetic objective lenses with saturated polepieces, Optik **57**, 9-34, 1980.
[9] K. D. van der Mast, C. J. Rakels and J. B. le Poole, A high quality multipurpose objective lens, Proc. Cong. on Electron Microscopy Vol. 1, The Hague 1980, pp. 72-73.

mediately above the polepieces of the objective and can be switched on or off (i.e. made optically active or inactive), depending on the required mode of operation. Normally, switching a lens off interrupts the current through the lens, which means that the heat-flow conditions are changed, and hence the dimensions. Near the specimen, however, the dimensions have to be highly stable, so that changes in heat flow are not permitted. The minilens is switched on and off optically without causing fluctuations in heat flow, by means of a special magnetic configuration in which the minilens is de-activated by *reversing* the current in the appropriate coil.

In this magnetic configuration the magnetic flux of the objective lens is split in such a way that about 50% of the action of the minilens is based on this flux and 50% on the flux from its own coil. In the left-hand half of fig. 7 the two fluxes in the 'air gap' of the minilens oppose one another. The resultant flux in the air gap is therefore zero and the minilens is optically inactive. In the situation shown in the right-hand half of fig. 7 the current in the coil of the minilens has been reversed, and the two fluxes in the air gap reinforce, so that the minilens is optically active. The flux of the objective lens is split by including an additional reluctance around the coil of the minilens. This reluctance and the 'air gap' of the minilens are formed by rings of non-magnetic material, such as aluminium or copper.

The unmodified symmetrical immersion objective is particularly suitable for making very small spots on the specimen. *Fig. 8a* shows the ray diagram for the smallest spot, the nanoprobe spot, used for scan images and for analyses. Here the electrons move parallel to one another between the second condenser lens (C_2) and the condenser part (O_u) of the objective. An incidental advantage of this objective is that there is a relatively large amount of space between the polepieces. A disadvantage of a symmetrical immersion objective without an additional condenser lens, however, is that when the instrument is used as a TEM the objective is less suitable for parallel illumination and defocused illumination, i.e. with the spot on the specimen slightly out of focus.

Fig. 8b shows that these disadvantages have been overcome by the addition of the minilens (C_m). When this lens is energized so that its focus coincides with that of the condenser part (O_u) of the objective, the result is a 'telecentric' optical system. The special feature of such a system is that a parallel incident beam leaves the system still as a parallel beam. Fig. 8b shows that, in spite of the presence of the converging lens O_u just above the specimen, parallel illumination of the specimen is nevertheless obtained. If the con-
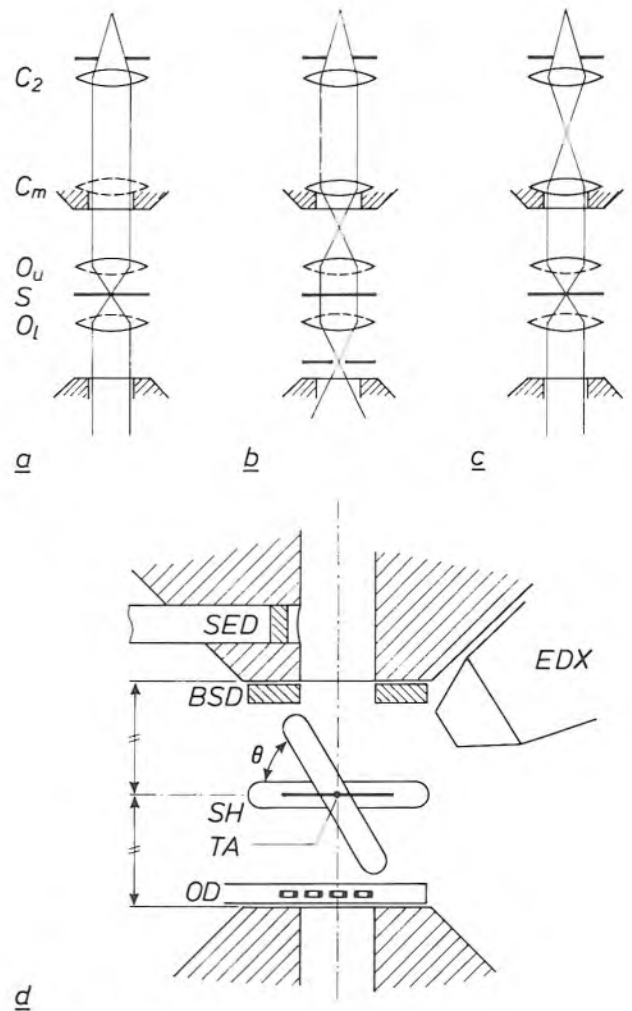

Fig. 8. The main operating conditions of the Twin objective lens. C_2 second condenser lens. C_m mini-condenser lens. O_u condenser lens formed by the magnetic field above the specimen S. O_l image-forming lens produced by the field below the specimen. *a*) Ray diagram when the smallest possible spot — the nanoprobe spot — is formed on the specimen. C_m is not in operation. *b*) Ray diagram for parallel illumination of the specimen. C_m and O_u together form a telecentric system. *c*) Ray diagram when C_2 is energized in another way, producing a larger spot — the microprobe spot — on the specimen. *d*) The detectors and holders that have to be accommodated between and in the polepieces near the specimen; see also caption to fig. 2. *SH* specimen holder, which can be tilted through an angle θ about an axis *TA* perpendicular to the plane of the drawing. *OD* holder for four different objective diaphragms.

denser lens C_2 is energized in another way a larger spot than the nanoprobe spot is produced on the specimen — the microprobe spot; see fig. 8c. Fig. 8a, b and c show three important modes of operating with the Twin lens. The ray diagrams are limiting cases for a large number of variations, e.g. with a defocused spot or with incompletely parallel illumination of the specimen.

The specimen is thus placed half-way between the polepieces of the objective lens, since with the easily switched mini-condenser lens a strong lens immediately above the specimen is no handicap. Fig. 8d shows that the relatively large free distance above and below

the specimen is used for accommodating a holder for four different objective diaphragms, the detectors for back-scattered electrons and emitted X-rays, and also for tilting the specimen holder through the largest possible angle. The detector for secondary electrons, which has an electrode at a potential of 10 kV to collect electrons with an energy of less than 50 eV, is accommodated in a radial hole in the upper polepiece. The specimen must be tilted:

• for investigating crystal structures with the aid of diffraction patterns;

• for making stereo micrographs, i.e. micrographs with opposite angles of tilt, but otherwise identical;

• for making series of micrographs with different tilt angles, from which a computer can reconstruct three-dimensional images, e.g. of biological macromolecules; and

• for obtaining maximum signals from the X-ray detector.

There is sufficient space for the X-ray detector to be mounted close to the specimen. The solid angle at which the detector 'sees' the specimen is therefore relatively large, and this also means that a strong signal is obtained from the X-ray detector, so that selective energy-dispersive analysis of the specimen is possible.

The designers of the objective described here were confronted with two conflicting requirements: they could have either a large space between the polepieces or a high resolution. Scaling down the polepieces reduces the space available, but gives a higher resolution because the spherical and chromatic aberrations will be smaller. On the other hand, a relatively large space between the polepieces gives a slightly lower resolution. The dilemma was resolved by making two versions of the objective lens, the Twin lens and the Super-Twin lens. In the first version the emphasis is on a large tilt angle, in the second on a high resolution with high magnification. *Table I* lists the focal distance, spherical and chromatic aberration, point and line resolution, minimum spot diameter and tilt angle for the two objectives.

Table I. Focal length f, constants C_s for spherical aberration and C_c for chromatic aberration[10], minimum spot diameter d, point resolution R_p, line resolution R_1 and maximum tilt angle θ for the Twin and Super-Twin objectives.

	Twin	Super-Twin
f	2.7 mm	1.7 mm
C_s	2.0	1.2
C_c	2.0	1.2
d	2.0 nm	1.5 nm
R_p	0.34 nm	0.30 nm
R_1	0.20 nm	0.14 nm
θ	$\pm 60°$	$\pm 15°$

Operating modes

With the versatile Twin lens and the deflection coils above and below the specimen the CM12/STEM microscope offers a large number of optical settings or modes. In this section we shall look at the most important of these modes, classified by the nature of the energization of the deflection coils.

The illumination of the specimen corresponds in general to fig. 8*a*, *b* or *c*, i.e. illumination with the nanoprobe spot, a parallel beam or the microprobe spot. The spots may be slightly defocused to cover a larger area of the specimen. We note in passing that the deflection coils above the specimen can also be used as a focusing aid with a standard TEM image, by energizing the upper coils with a square-wave voltage and situating the pivot point *PP* in the specimen, as shown in fig. 6*d*. The user then sees two images, and the image-forming system is correctly focused when the two images coincide. This 'wobbling' illumination procedure considerably simplifies the focusing[10].

Modes with no dynamic energization of the deflection coils

These modes include the conventional TEM modes. They consist of a high-magnification mode TEM-HM and a low-magnification mode TEM-LM. In the TEM-HM mode the objective is always energized and most of the other image-forming lenses are energized; the image is focused by varying the current through the objective. In the TEM-LM mode the objective is only weakly energized, so that really the diffraction lens is the first image-forming lens. The image is therefore focused by varying the current through the diffraction lens. With central illumination a bright-field image is obtained, and with tilted illumination a dark-field image. In the latter case the electrons that are not scattered in the specimen are intercepted in TEM-HM by the objective diaphragm. In tilted illumination the deflection coils above the specimen are therefore *statically* energized.

An image of the electron diffraction pattern at the back focal plane of the first image-forming lens can be obtained both in the TEM-HM and in the TEM-LM mode. The other image-forming lenses are then energized so as to produce an image corresponding to this focal plane on the fluorescent screen. In the TEM-HM diffraction mode the SA diaphragm (see fig. 5) can be used to select a part of the ordinary image of the specimen for closer investigation of the crystal structure.

Element analysis can be carried out in the nanoprobe mode. Since the spot at the specimen is extremely small (fig. 8*a* and Table I) it is then possible to ana-

[10] C. E. Hall, Introduction to electron microscopy, McGraw-Hill, New York 1953.

lyse the X-radiation originating from a very small part of the specimen. Here the energy-dispersive X-ray detector *EDX* is used; see fig. 8*d*. The energy distribution of the X-radiation permits qualitative and quantitative analysis of the elements in the specimen.

Sensitive specimens can be analysed in the low-dose mode. This can be done for ordinary micrographs, diffraction micrographs and even with STEM, which will be discussed below. The procedure is as follows. At low electron density and low magnification an interesting part of the specimen is identified. The specimen is not displaced further and with high magnification and at the normal electron density — which might cause local damage to the specimen — a part *next to* the interesting part is observed; the image is then focused. During this procedure the deflection coils above and below the specimen are energized statically (fig. 6*b*), in such a way that the lateral displacement of the beam above the specimen is compensated beneath it. Finally, without energizing the deflection coils and without refocusing, the actual exposure on the photographic plate is made. The interesting part of the specimen that produces the image then lies on the optical axis of the microscope again.

Diffraction patterns can be obtained not only in the conventional way by illuminating the specimen with a parallel beam but also by using a convergent beam. According to W. Kossel and G. Möllenstedt this gives a CBED pattern (CBED is the abbreviation for convergent-beam electron diffraction) built up from 'patches' instead of points [11]. The patches have a structure that carries additional crystallographic information. The use of a convergent beam in diffraction has the further advantage of providing information about a very small part of the specimen.

An important mode for users who wish to depart from the programmed settings for electron-optical experiments is the free-control mode. In this mode the user can vary the currents through the separate lenses as he wishes.

Modes with the upper deflection coils dynamically energized

The upper deflection coils are mainly used when the instrument is used as a scanning-transmission electron microscope (STEM). The spot then describes a rectangular pattern across the specimen, and the video signal supplied to one of the monitors on a control panel (fig. 4) is modulated by a detector signal. The detectors situated above the specimen can be seen in fig. 8*d*. Their output signals correlate with the number of secondary electrons, the number of back-scattered electrons or the X-ray intensity. *Fig. 9* shows that a signal can also be used that correlates with the number
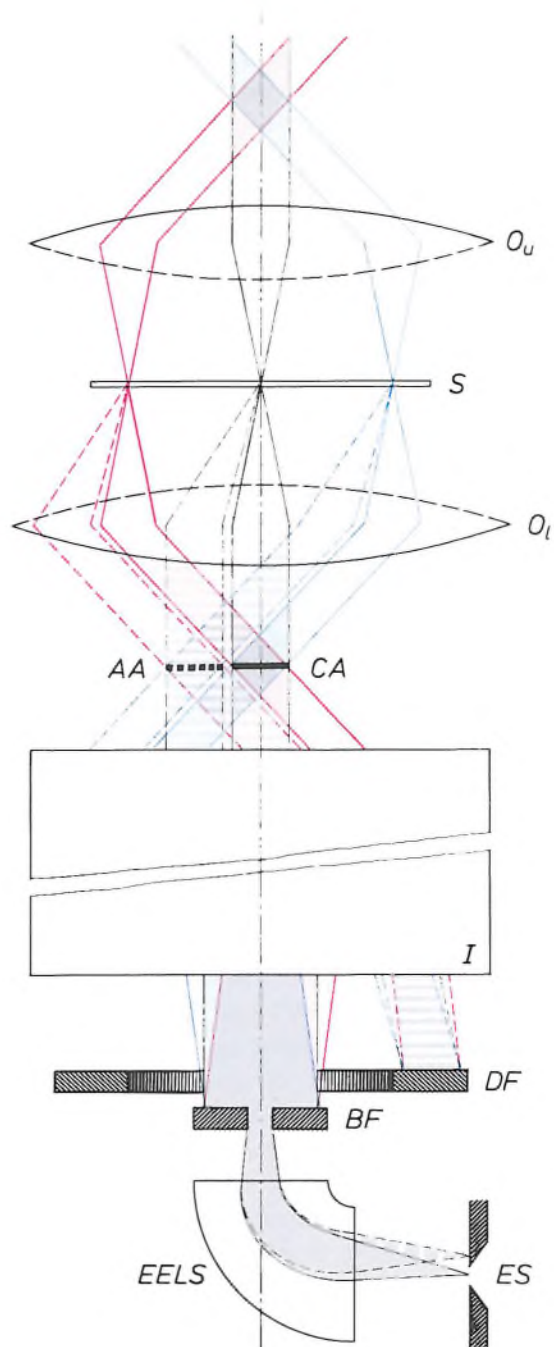

Fig. 9. Ray diagram for use of the microscope as a STEM, using the detectors in the projection chamber; see also figs 2 and 5. *I* imaging lenses below the objective. The grey, red and blue beams correspond to different positions of the spot, which describes a line across the specimen *S*. The beams defined by the continuous lines are not scattered in the specimen; they all pass through a circular area *CA* in the back focal plane of O_l. The beams defined by the dashed lines are scattered at a particular angle in the specimen; they all pass through an annular area *AA*, which is concentric with *CA*. A STEM bright-field image can thus be obtained with the signal from detector *BF*, and a STEM dark-field image with the signal from detector *DF*. In the *EELS* detector electrons with a high kinetic energy are not deflected so much in a magnetic field perpendicular to the plane of the drawing as electrons of low energy. The electrons can thus be sorted by energy. *ES* exit slit of the detector.

of electrons transmitted through the specimen. *Fig. 10a* shows the corresponding ray diagram when the nanoprobe spot is used.

Fig. 9 demonstrates the advantages of a symmetrical immersion objective when the instrument operates as a STEM. When a parallel beam is incident on the condenser part (O_u) of the objective a parallel beam emerges from the objective part (O_l), since the specimen is located in the common focal plane. In addition to non-scattered beams there are also scattered beams emerging from the objective. All the non-scattered beams pass through the same circular area in the back focal plane of the objective part. All the beams scattered at a particular angle pass through an annular area concentric with the first one. The special feature is that these areas do not move when the spot travels across the specimen.

Since the lens system forms an image of both the circular area and the annular area, it is in general possible to measure the intensities of transmitted non-scattered and scattered beams. This is done with the detectors *BF* and *DF* in the projection chamber (fig. 9). The corresponding video signals produce a STEM bright-field image or a STEM dark-field image on a monitor. The transmitted electrons can also be sorted by energy with an EELS detector (EELS stands for electron energy-loss spectroscopy); we shall return to this presently.

In the SEM and STEM modes a choice can be made between high-magnification (HM) and low-magnification (LM) modes. In the S(T)EM-HM mode the nanoprobe spot (fig. 10a) is used, with the fineness of the raster pattern on the specimen adapted to the size of the spot. In the S(T)EM-LM mode a coarser pattern and a much larger spot are used. This is done by switching off the objective and focusing the illuminating beam with the condenser lens C_2 (fig. 5).

Another mode is the TEM dark-field mode with conical illumination. The incident beam is tilted over a preset angle (fig. 6d) and then rotated continuously about the optical axis. On a photographic plate a kind of superimposition of dark-field images is obtained, since all the azimuthal angles of the illuminating beam are described. The advantage of this is that more details can be seen in the image than in an ordinary dark-field image, since the details are illuminated from many more directions.

Modes with the lower deflection coils dynamically energized

In the SCIM mode (SCIM: scanning in imaging) the image of the specimen is scanned with the aid of the lower deflection coils, see fig. 10b, making use of detector *BF* in the projection chamber. In the SCID
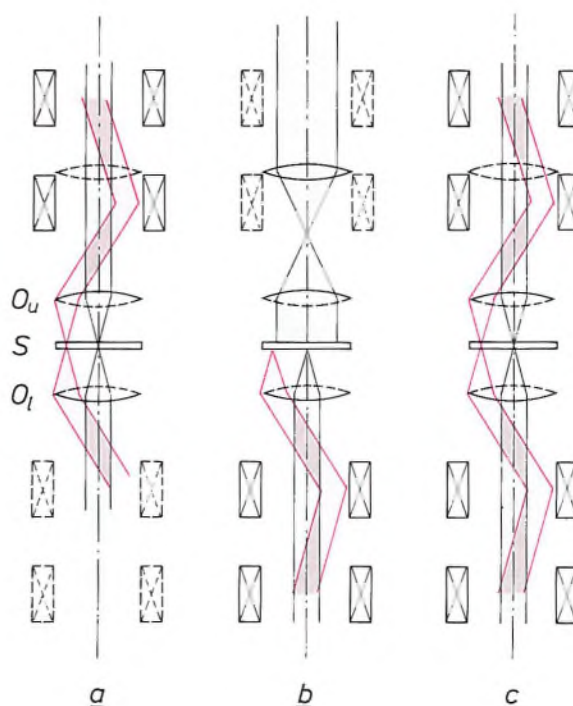

Fig. 10. Ray diagrams in different modes, when *a*) only the deflection coils above the specimen *b*) only the deflection coils below the specimen, and *c*) the deflection coils above *and* below the specimen are used. The ray diagram in (*a*) is the one used for the nanoprobe spot in STEM. The ray diagram in (*b*) is the one used for scanning the specimen from below; the signal from detector *BF* (fig. 9) can then be converted into a video signal for one of the monitors. The ray diagram in (*c*) is the one used in the low-dose mode, when the coils are statically energized. When the coils are dynamically energized, this is the ray diagrams for use as a STEM with the *EELS* detector; see also fig. 9. The deflection of the beam above the specimen is then compensated below it.

mode (SCID: scanning in diffraction) the image of the diffraction pattern is treated in the same way. In these forms of scanning, the image of the specimen or the diffraction pattern moves across the detector. The result presented on a monitor is comparable with an ordinary TEM micrograph. The advantage of this procedure is that the video signal can be processed electronically. If the analog video signal is converted into a digital signal with an A/D converter, the signal can also be processed numerically.

Modes with the upper and lower deflection coils dynamically energized

In the EELS detector (fig. 9) the electrons transmitted through the specimen are deflected through an

[11] G. Möllenstedt, Über die chromatischen Verluste von Elektronen beim Durchtritt durch Materie, Optik 9, 473-480, 1952;
G. Thomas and M. J. Goringe, Transmission electron microscopy of materials, Wiley, New York 1979;
M. N. Thompson, A review of TEM microdiffraction techniques, Philips Electron Opt. Bull. EM 110, 31-39, 1977;
J. W. Steeds, Convergent beam electron diffraction, in: J. J. Hren, J. I. Goldstein and D. C. Joy (eds), Introduction to analytical electron microscopy, Plenum, New York 1979, pp. 387-422.

angle of about 90° in a magnetic field. The angle of deflection depends on the energy of the electrons: high-energy electrons are deflected less than those with low energy. At a particular current through the magnetic coil the electrons passing through the output slit have a particular energy, so that the electrons at the input of the detector can be sorted by energy by varying the current. These electrons always have to pass through the aperture in the partition diaphragm (*PD* in fig. 5) below the second projector lens, which separates the vacuum of the column from that of the projection chamber. At the input of the EELS detector, however, the electrons must all have the same direction. If the EELS detector is to be used for making a STEM micrograph, the deflection due to the upper deflection coils must therefore be compensated by an equal and opposite deflection due to the lower deflection coils; see fig. 10*c*. The ray diagram is comparable with that in the low-dose mode, but there the deflection coils are not used dynamically but statically.

The control system

The user communicates with the instrument by means of controls that adjust quantities such as currents in lenses, deflection coils and stigmator coils and d.c. voltages in the electron gun. As a result a picture appears on the screen in the projection chamber, photographic material is exposed or an image is formed on a monitor screen. In earlier microscopes there were fixed connections between almost every coil or electrode in the microscope column and one or more controls on the control panels. This meant that there were very many manual controls, and the user had to be thoroughly familiar with the consequences of varying any particular current or voltage.

The new microscope discussed here has some manual controls and a control screen for communication with the user; see *fig. 11a*. The screen shows the mode the instrument is operating in and the settings of various optical parameters. On each side of the screen there are eight controls, called 'soft keys', whose function is determined by the control software. The information on the screen, which is called a 'page', indicates the function of these soft keys; see fig. 11*b*. The other controls on the control panels do not in general have any fixed connection with the microscope column either. When a control is operated, it delivers one or more electrical pulses, which are converted into a command to the control software. The controls are therefore usually associated with a function. The principal functions are magnification, image brightness and focus. In addition to the soft keys there are two 'ordinary' controls whose function is not fixed

Fig. 11. The user communicates with the instrument by means of *a*) the controls on the panels and *b*) the soft keys on either side of the control screen. Information displayed on the screen includes the name of the mode in which the microscope is operating and the parameter settings.

but can be changed. These are the multifunction controls, which are mainly used for alignment of the microscope column; their function is indicated by the pages relating to the alignment procedure.

The control software guides the user to his goal — a micrograph or an analysis — via the pages on the screen and the controls on the panels. The user does not therefore need to know as much about the optical structure of the instrument as he did with previous instruments. *Fig. 12* gives an idea of the hierarchy of the pages that the user can call to the screen. The figure gives four levels. (The particular pages shown refer to a simpler version of the microscope, with a limited range of mode options.)

The page from level *1* shows a menu with four options. If the user selects the option MODES, the screen then shows the page MODE SELECTION from level *2*. The menu now gives options for the modes that are available with the particular version of the instrument, and the option CONFIGURATION, which shows a page that displays the features of the instrument. (This page shows here that the user has placed an electron gun with a tungsten cathode, not
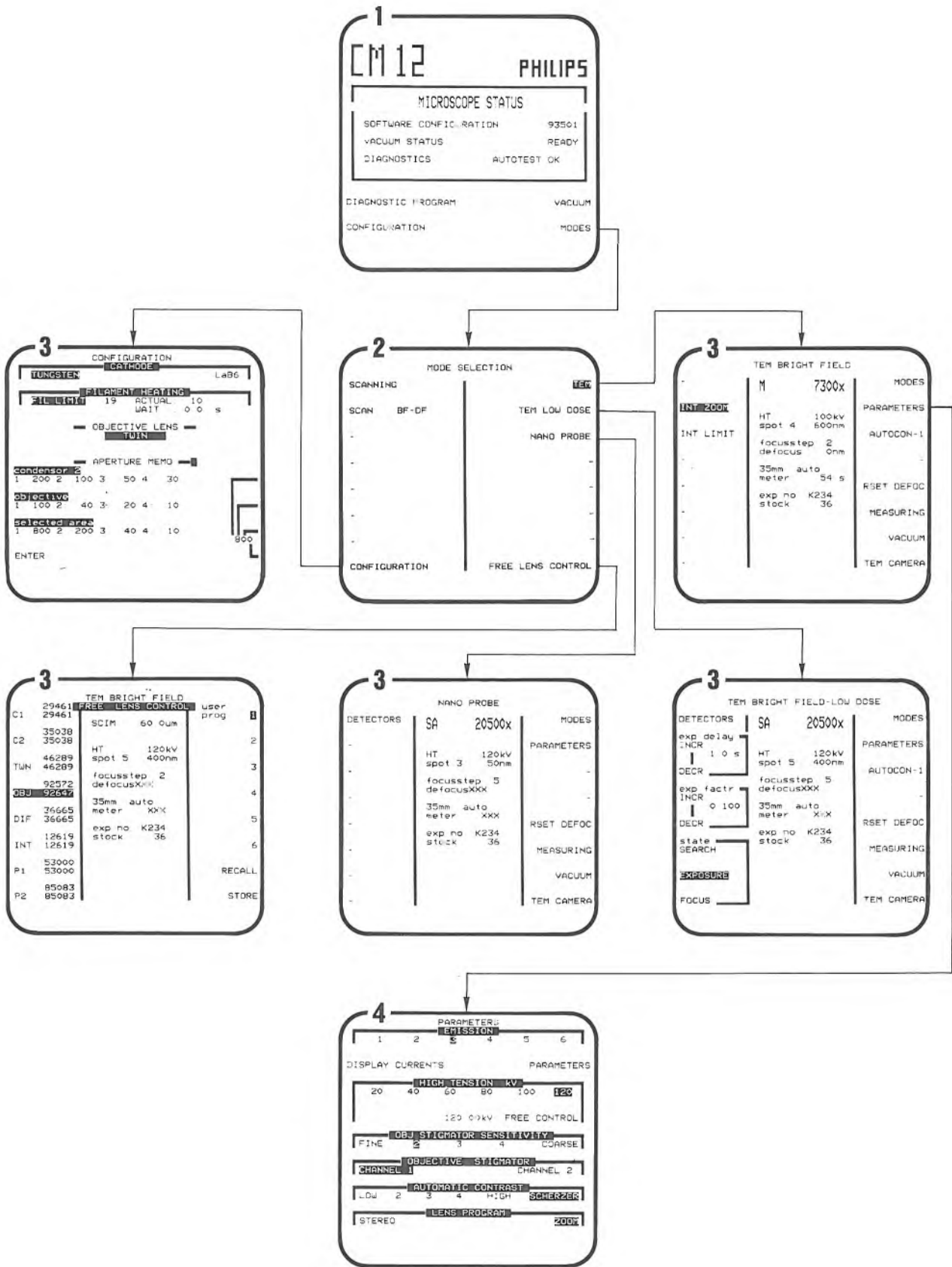
Fig. 12. The hierarchy of some of the many 'pages' that can be displayed on the control screen. The number at the upper left of each page indicates the level. The mode is selected from the options on a page at level 2. The mode to which the instrument is set can be seen from a page at level 3. The field in the centre then gives the settings of the parameters; the fields on either side indicate the functions of the soft keys. Parameters are changed via a page at level 4.

an LaB₆ cathode, in the microscope.) The pages at level *3* associated with the various modes show at the centre the settings of parameters such as the 'high tension' and spot size. The functions of the sixteen soft keys are indicated on the left and right. If the user presses the soft key PARAMETERS, the screen displays the relevant page of level *4*. This indicates the options selected for the parameter values (dark against a light background) and the options still open (light against a dark background). Options previously selected can be changed by pressing one of the two soft keys on the appropriate line. The user can return to a page at the preceding level by pressing the key READY at the bottom of the screen; see fig. 11*b*. Light-emitting diodes (LEDs) indicate whether this key or other keys are 'active'.

The heart of the control system is a 16-bit microprocessor, the INTEL 8086. To gain computing speed and accuracy this microprocessor works in conjunction with a numeric data processor, the INTEL 8087. This can process floating-point numbers between 8.43×10^{-37} and 3.37×10^{38} to an accuracy of seven decimal places. The 8086 microprocessor processes the commands given by the user or by sensors with the RMX 88 operating system. The operating system ensures that the commands are dealt with virtually in real time. All the computed results are transmitted every 15 ms in order of importance, under the control of an external clock signal. The two processors and the input and output units interact via an IEEE 796 bus system. The 8086 processor communicates with the various electronic circuits through a bus system that we have designed. This bus system is insensitive to interference (from high-voltage flashover for example). This insensitivity is largely due to the use of optical couplings.

As an example we shall show, with reference to *fig. 13*, how the current in the deflection coils above and below the objective is controlled. In general this current is equal to the sum of a direct current used for correcting the beam direction and a sawtooth alternating current used for scanning. The current in the deflection coils must be very accurately controlled to avoid unacceptable movement of the image.

The circuit for generating the current through the deflection coils is designed in such a way that a digital signal from the control system is multiplied by an analog signal in two digital/analog converters. In one digital/analog converter the digital signal D_{DC} is multiplied by an accurate direct voltage V_{ref}. In the other digital/analog converter the digital signal D_{AC} is multiplied by an accurate sawtooth voltage V_{ST}. Multiplication can be performed in four quadrants, so that for example two negative signals multiplied together
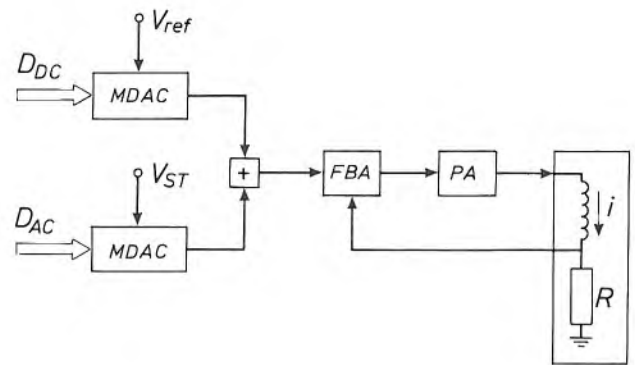

Fig. 13. Diagram of the current control in a set of deflection coils above or below the objective. *MDAC* multiplying digital/analog converters. D_{DC} and D_{AC} digital signals from the control system. V_{ref} accurate direct voltage. V_{ST} accurate sawtooth voltage. *FBA* feedback amplifier. *PA* power amplifier. Both amplifiers are part of a control network that includes the deflection coils. The value of the current *i* in these coils is fed back as a voltage across a resistor *R*.
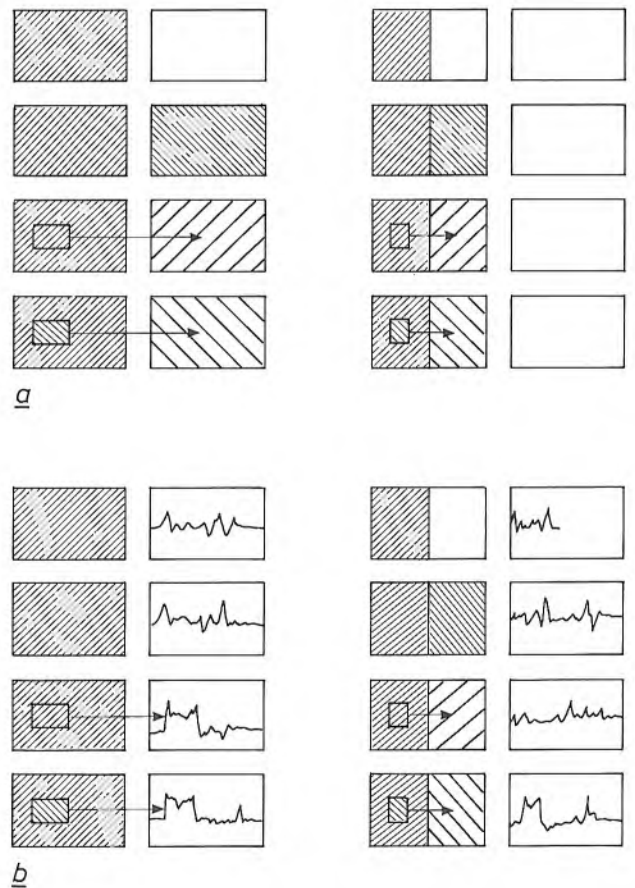

Fig. 14. STEM results displayed on the two monitor screens. Images are indicated by hatching. The same images have the same direction of hatching; coarser hatching indicates higher magnification. *a*) One image or two images on each screen or on each half of the left-hand screen. An image can be projected into the other image at a different magnification. Fig. 19 shows an example for the choice given schematically at the lower right. *b*) One image or two images on the left-hand screen only. The right-hand screen displays the brightness variation of one line as a curve. The curve may also be displayed on the 'videoscope', fitted to the microscope as an accessory; see fig. 4*a*.

give a positive signal. The product signals are then added. The result acts as a reference signal in a control network, which includes a feedback amplifier and a power amplifier. The power amplifier supplies a current i to the deflection coils. The value of the current is fed back into the control network as a voltage across a resistor.

The period of the sawtooth voltage V_{ST} in fig. 13 is between 1 and 1000 ms, or is equal to the line period in one of the television standards. The amplitude of the analog sawtooth signal is digitally calibrated by the control system every time the microscope is switched on. Because of this automatic calibration the advantage of digital electronics — accuracy — is combined with that of analog electronics — speed.

In the STEM modes the video signals for the two monitors (see fig. 4a) are derived from one or more detector signals. The video signals are the result of such operations as amplification, switching, mixing and filtering. These operations have to take place in a large bandwidth (up to 10 MHz) without the occurrence of noise or distortion due to overloading. This difficult problem has been solved by means of constant-current-source technology, also used in high-frequency oscilloscopes. The signal from the detectors is converted into a current that appears to come from
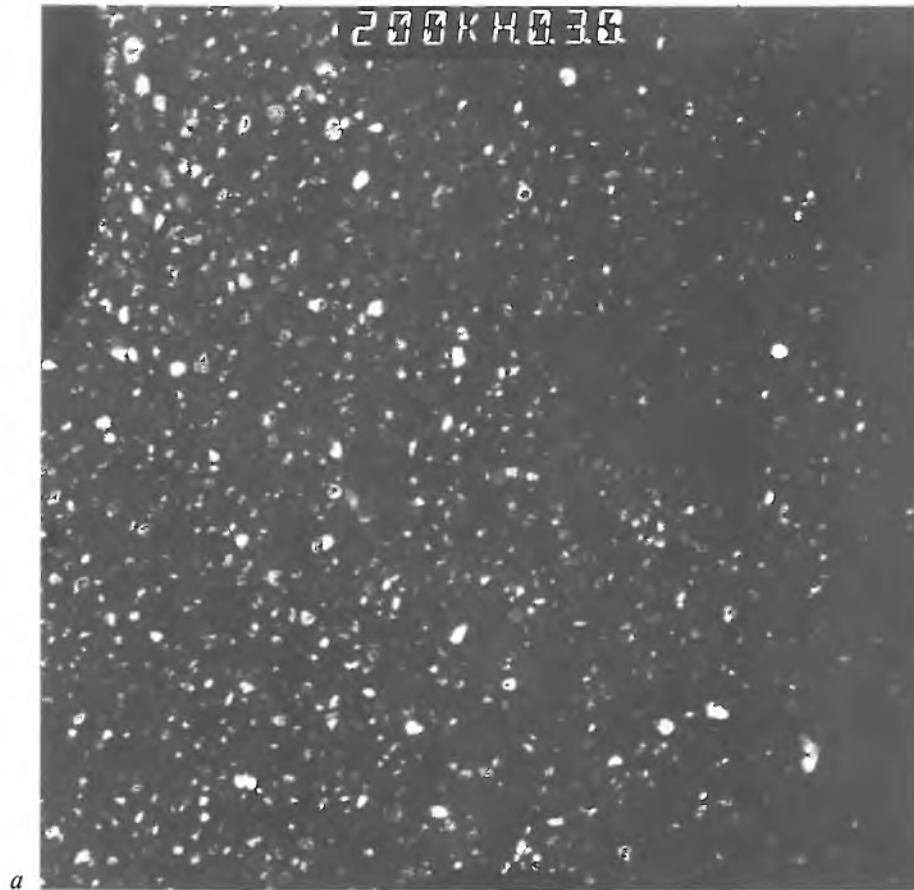
a source with an infinitely large internal impedance. There are two channels for video signals, so that the two monitors can be operated separately. The channels can also be combined in a variety of ways, and different magnifications can be selected for the monitors. One screen may be divided into two halves, so that each half shows the signal from one channel; see *fig. 14a*. If required, a monitor can display the video signal of one line as a curve; see fig. 14b.

Some results of investigations made with the microscope

To conclude, we shall illustrate the versatility of the CM12/STEM microscope with a number of micrographs of different specimens, made in different modes. The corresponding page on the screen is shown with each picture. *Fig. 15* is a TEM micrograph of a gold particle vacuum-evaporated on a film of amorphous carbon. Twinning structures are visible in the gold particle. The micrograph was made with the Super-Twin objective at a magnification of about 8×10^6. More important than the magnification is the resolution achieved. The spacings of the $(1\bar{1}1)$ planes and the spacings of the $(11\bar{1})$ planes in the crystal lattice (the value is 0.235 nm) appear to be visible. Since
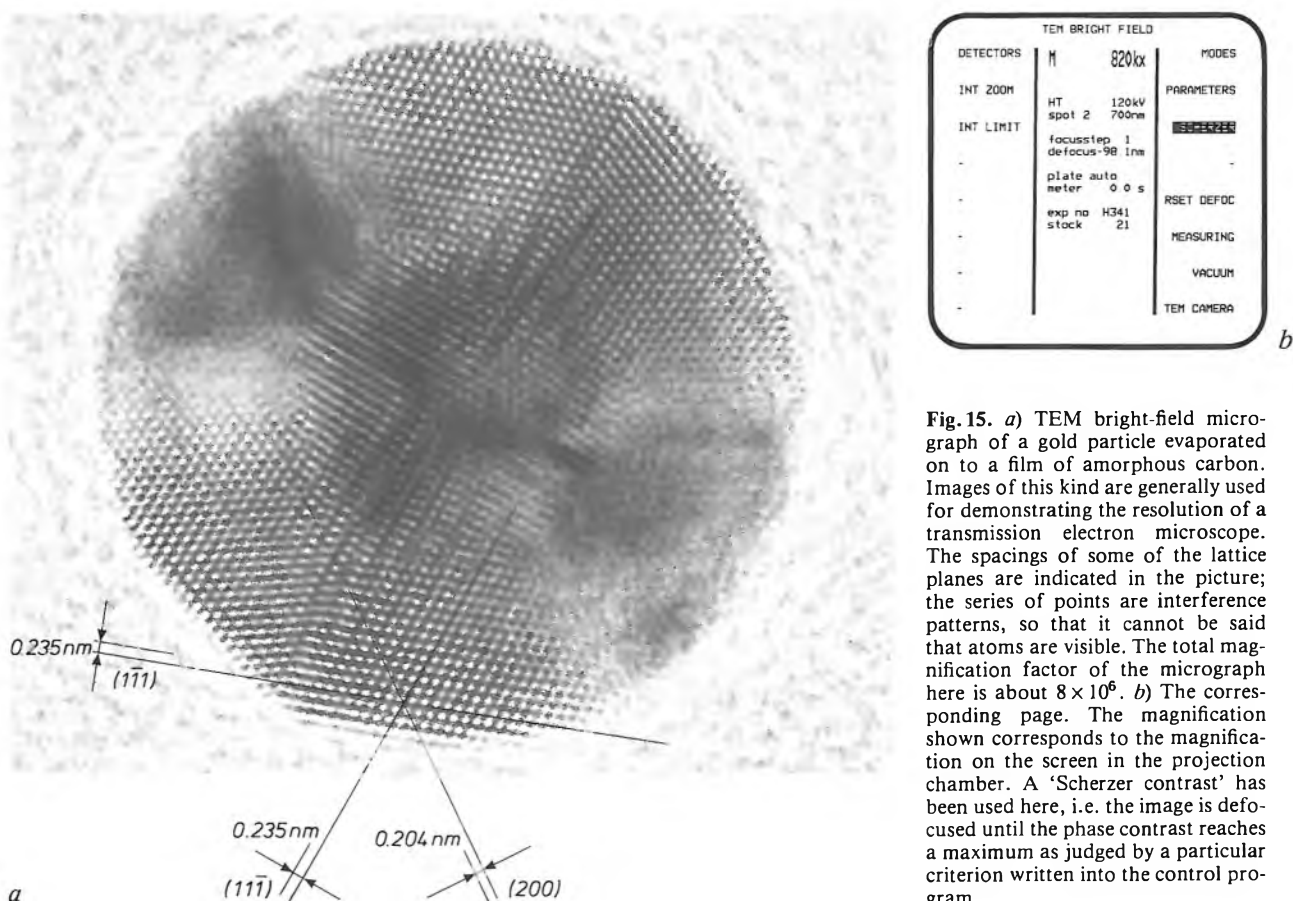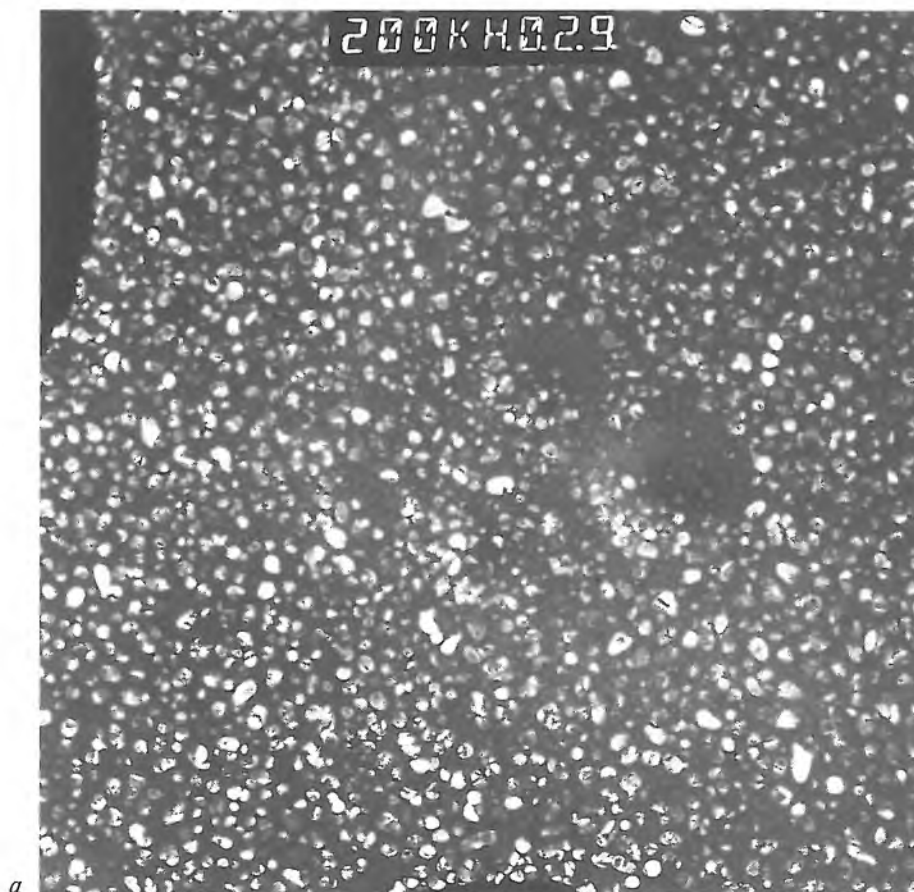
Fig. 15. *a*) TEM bright-field micrograph of a gold particle evaporated on to a film of amorphous carbon. Images of this kind are generally used for demonstrating the resolution of a transmission electron microscope. The spacings of some of the lattice planes are indicated in the picture; the series of points are interference patterns, so that it cannot be said that atoms are visible. The total magnification factor of the micrograph here is about 8×10^6. *b*) The corresponding page. The magnification shown corresponds to the magnification on the screen in the projection chamber. A 'Scherzer contrast' has been used here, i.e. the image is defocused until the phase contrast reaches a maximum as judged by a particular criterion written into the control program.

Fig. 16. *a*) TEM dark-field micrograph of the same type of gold particles as in fig. 15, but now at reduced magnification. Not all of the particles are visible (see fig. 17) because the illumination was from one side. *b*) The corresponding page. The tilt angle of the illumination can be calculated from the tilt angles in the *x*- and *y*-directions, stated at the bottom of the page. The user can select a different azimuthal angle if desired.

Fig. 17. *a*) Micrograph comparable with the one in fig. 16 but now with conical illumination. The tilted illuminating beam rotated continuously about the optical axis. Since the illuminating beam passed through all azimuthal angles, nearly all the gold particles are visible. *b*) The corresponding page.
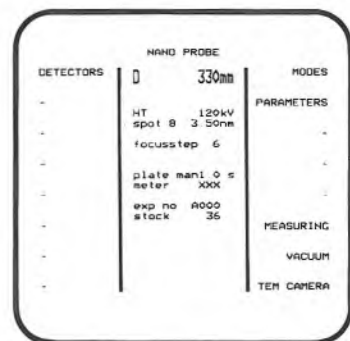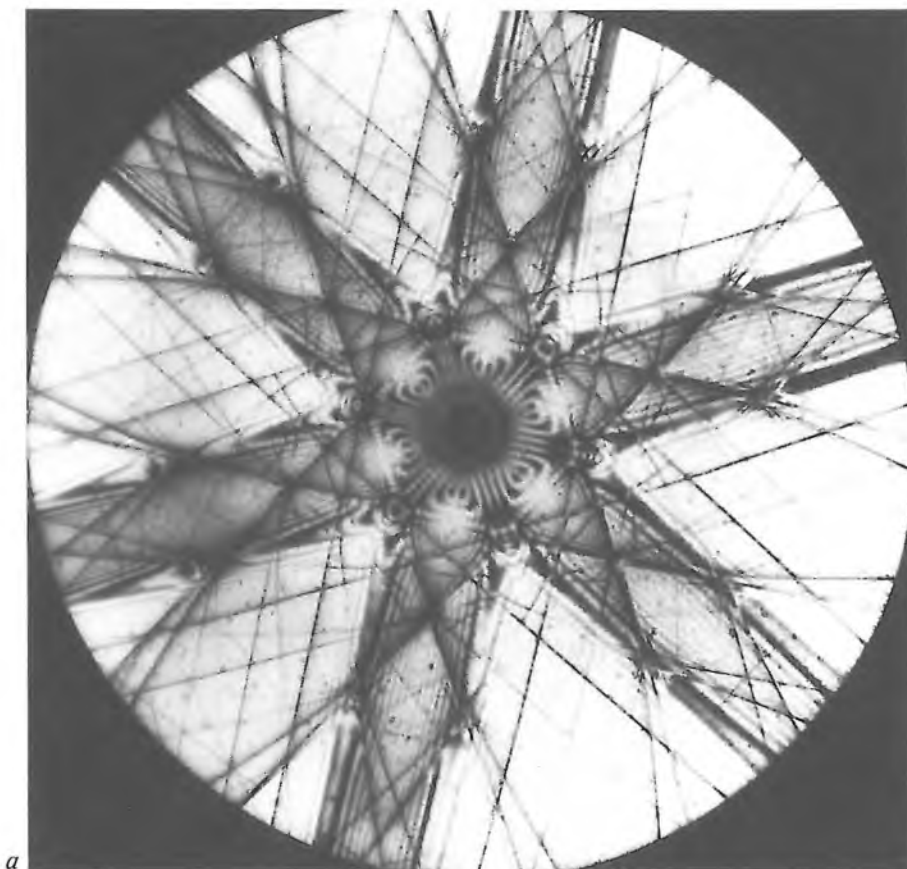
Fig. 18. *a*) Micrograph of a CBED pattern (CBED: convergent-beam diffraction pattern[111]) of single-crystal silicon. Because of the [111] orientation of the specimen surface a 120° symmetry can be observed. *b*) The corresponding page.

the intersection of these planes with the plane of the micrograph is 'visible' — in fact, interference patterns are observed — there is also an indication of the intersection with the (200) planes, whose spacing is 0.204 nm.

Fig. 16 shows a TEM dark-field micrograph of the same amorphous carbon film with gold particles, but now at a lower magnification. For comparison *fig. 17* shows a TEM dark-field micrograph with conical illumination of the same specimen, made with the tilted beam rotating continuously about the optical axis. More particles are visible in fig. 17 than in fig. 16, because for fig. 16 the specimen was illuminated from one direction only. In the case of fig. 17 the illuminating beam passed through all possible azimuthal angles.

Fig. 18 shows a CBED pattern, where the illuminating beam converges so as to make the spots of the diffraction pattern overlap completely. The resulting complicated pattern[111] gives information about the symmetries in the crystal structure, here of single-crystal silicon with [111] orientation. Observation of the cubic structure of silicon in the [111] direction reveals a 120° symmetry. The specimen is locally 100 to 200 nm thick. This was achieved by ion-etching a silicon wafer a few microns thick until it was so thin that a small hole appeared in it. The diffraction micrograph corresponds to a 'wedge' of material next to the
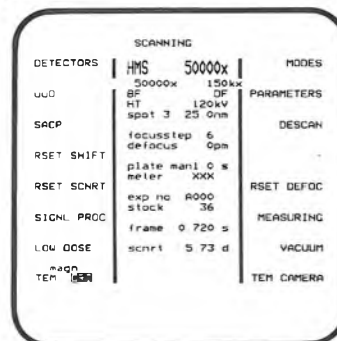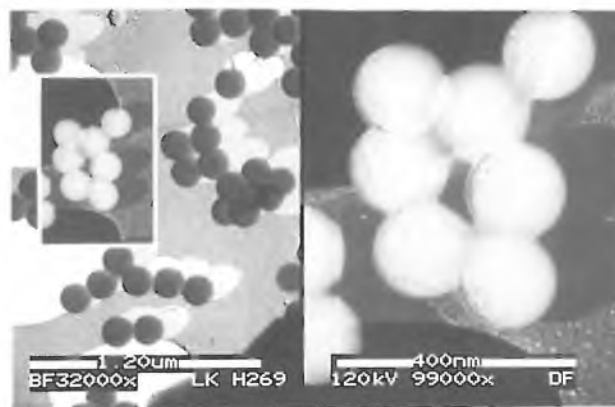

Fig. 19. *a*) STEM-HM micrograph of latex spheres. Gold has been evaporated on to the specimen from one direction. On the left-hand half of the screen there is a bright-field image, on the right-hand half a dark-field image. The image on the right is projected into the left-hand image at a different magnification. *b*) The corresponding page.
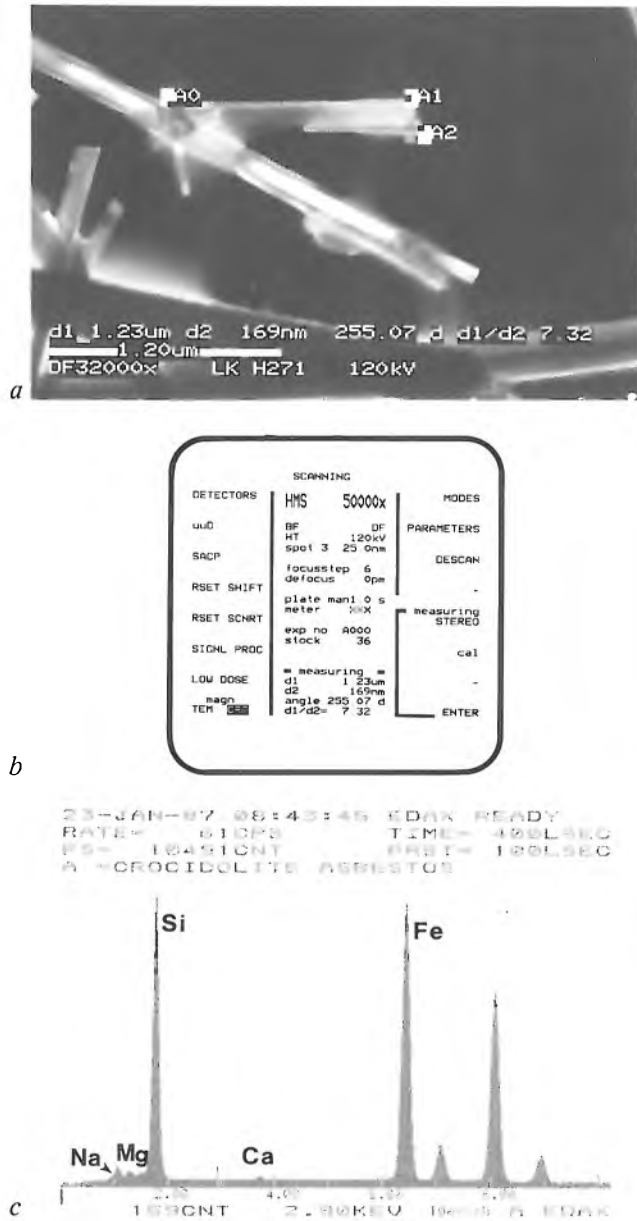
Fig. 20. *a*) STEM-HM micrograph of crocidolite fibres. To confirm that we are dealing with asbestos, the length/breadth ratio d_1/d_2 was determined. This ratio was calculated by the software and shown in the micrograph. *A0, A1* and *A2* are reference points for the measurement. The micrograph also gives the measured lengths of d_1 and d_2, corrected for the magnification, and the angle between d_1 and d_2. *b*) The corresponding page, also with the measured results. *c*) Spectrum taken with the energy-dispersive X-ray spectrometer, showing the peaks for the elements that are characteristic of crocidolite. The three peaks on the right are a second Fe peak and Cu peaks, originating from copper in the specimen gauze.

Fig. 21. SCID micrograph (SCID: scanning in diffraction) of a MoO$_3$ crystal. *a*) Image on the monitor screen, which is comparable with an electron-diffraction micrograph taken with one of the two cameras in the projection chamber. *b*) Almost the same image, but now with an extra vertical deflection for each line, which is proportional to the brightness in (*a*). The relative brightness, and hence the relative value of the detector signal, can thus be measured in the image. *c*) The corresponding page.

hole. Micrographs of this kind are very useful in the study of silicon since dopants show up as changes in the pattern.

Fig. 19 shows a STEM-HM micrograph of tiny spheres of latex. To obtain a shadow effect, gold was evaporated on to the specimen from one direction. The gold particles on the specimen are comparable with those in figs 15, 16 and 17. Specimens of this type are widely used in scanning electron microscopy for checking the resolution. The left-hand half of the monitor screen shows a bright-field image, the right-hand half a dark-field image. The image on the right was projected at a different magnification into the image on the left. The method of splitting the screen corresponds with that shown on the lower right in fig. 14*a*.

Fig. 20 shows how the presence of asbestos, whose harmful effects are well known, can be demonstrated. Fig. 20*a* is a STEM-HM dark-field micrograph of fibres of blue asbestos (crocidolite), one of the most harmful forms of asbestos. Crocidolite has the formula $Na_{2-x}Ca_{0.5x}(Mg,Fe^{2+})_{3+1.5x}Fe^{3+}_{2-x}Si_8O_{22}(OH)_2$. The micrograph also presents the result of a method of measuring the dimensions of one of the fibres. A distance in the image can be defined by positioning a cross-wire, pressing a button, then repeating this at another setting. In this micrograph, and also on the page in fig. 20*b*, the length and breadth of the fibre are displayed, with their ratio and the angle in degrees between the directions of measurement. The length/breadth ratio, which should be at least 3, is extremely important in the characterization of asbestos. The measurement of this ratio and fig. 20*c*, which shows the spectrum measured with the energy-dispersive X-ray detector, confirm that this is a micrograph of crocidolite. (The three unnamed peaks on the right of fig. 20*c* are a second Fe peak and two peaks due to Cu in the gauze supporting the specimen.)

Fig. 21 shows SCID micrographs of single-crystal molybdenum oxide (MoO_3). The monitor image in fig. 21*a* is comparable with a normal diffraction pattern. One of the bright spots is the zero-order image of the electron source; the other spots are images of higher order. The distance between the spots is a measure of the lattice constant of the crystal. Fig. 21*b* shows the monitor image obtained when the detector signal is not used for modulating the intensity of the electron beam in the monitor tube but for producing extra vertical deflection of the beam. In this way the relative value of the detector signal can be measured in the monitor image. The changeover between this picture and the previous one is not made via the page on the control screen, as in fig. 21*c*, but by means of a key.

Summary. The CM12/STEM electron microscope has a Twin objective and microprocessor control. With this special objective it is possible to switch over quickly from a conventional TEM mode, with a direct image of the specimen or diffraction pattern on a fluorescent screen in the projection chamber, to a STEM mode, where the specimen is scanned by the illuminating beam and a detector signal is converted into a video signal for one of the monitors. Because of the special magnetic configuration of the objective, which includes a mini-condenser lens, this switch-over produces hardly any change in the heat-flow conditions in and around the polepieces. The CM12/STEM is very much easier to operate than other microscopes because the microprocessor guides the user to the various operating modes and features by providing information on a control screen. The use of 'soft keys' and multi-functional controls on the panels keeps the number of manual controls relatively small. Micrographs demonstrate the resolution and some of the many features of the instrument.

292

Philips Tech. Rev. **43**, No. 10, 292-302, Nov. 1987

Noise due to optical feedback in semiconductor lasers

B. H. Verbeek, D. Lenstra and A. J. den Boef

Wave reflection of signals into a device in which they are amplified can have considerable effects on its operation. A typical example is acoustic feedback with a microphone. An effect not so well known, but just as undesirable, is the fluctuation in the optical power of a laser because of reflected radiation. Since reflected radiation is an essential feature in many applications of semiconductor lasers, that radiation may lead to problems in the laser cavity.

Introduction

After the construction of the first working lasers in the early sixties, there was much speculation about the potential uses of the new radiation source. They ranged from 'science-fiction' applications to machining aids and distance measurements. While many of the uses envisaged at that time have since materialized, no-one could then have foreseen the scale on which lasers would be used in a wide variety of consumer products as well as in scientific equipment. Semiconductor lasers are used today as light sources in optical communications and in Compact Disc and LaserVision players. A problem that can arise in such applications is the fluctuation in intensity that can occur if radiation is reflected back into the laser cavity. Some aspects of this optical feedback will be dealt with in this article.

Laser action is based on stimulated emission, a process in which a photon of energy $h\nu$ stimulates electrons that are in an energy state E_1 to return to a state of lower energy E_2, with the emission of a photon such that $E_1 - E_2 = h\nu$; see *fig. 1*. The emitted photon has the same energy and phase and moves in the same direction as the original photon, and in its turn can cause further stimulated emission. To obtain the highest possible stimulated emission the photons are reflected back and forth through the material a number of times from two reflecting surfaces. These reflecting surfaces define the boundaries of the laser cavity. (Since we shall refer to an external feedback reflector later, we shall call this cavity the internal cavity.) The two reflecting surfaces allow some of the radiation to pass through, giving a beam of coherent radiation that only contains energy at the frequencies that lead to constructive interference on repeated reflection (the longitudinal modes). A necessary condition is that there should be more electrons available in the high energy level than in the low one (population inversion). This condition can be met in a number of ways. In a solid the population inversion can be brought
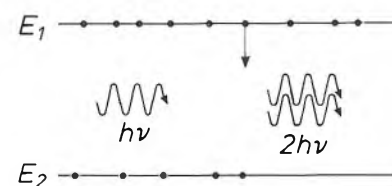
Fig. 1. Laser action can occur when the energy level E_1 of the atoms or molecules of a material contains more electrons than the lower energy level E_2. An incident photon of energy $h\nu = E_1 - E_2$ causes the emission of a second photon with the same energy and phase as the original photon.

Dr B. H. Verbeek and Ing. A. J. den Boef are with Philips Research Laboratories , Eindhoven; Dr D. Lenstra is with the Department of Physics at Eindhoven University of Technology.

about by intense light flashes. In a gas it results from collisions with accelerated electrons or with fast molecules or atoms. The inversion in semiconductor lasers is achieved by injecting charge carriers into a pn junction.

Briefly, the operation of a semiconductor laser is as follows; see *fig. 2*. A current in a pn junction in a direct [1] semiconductor causes electrons to flow from the conduction band in the n-type material towards the conduction band in the p-type material. These electrons can recombine with holes in the p-type material, with the emission of photons. Above a certain current stimulated emission occurs. The optical power of the laser can be directly controlled by varying the current.

Semiconductor lasers are now more and more widely used in various kinds of business and professional applications. This is because they are small and robust, are not so expensive as other types of lasers, and are easy to use.

An important application of semiconductor lasers is in information read-out in Compact Disc and Laser-Vision players. In these players the laser light is focused on the reflecting layer of the disc. The information is contained in the disc in the form of pits with a depth of about $\frac{1}{4}\lambda$ (λ is the wavelength of the laser light). The intensity of the reflected light is detected by one or more photodiodes. The pattern of the pits on the disc is represented in the detector signal by the difference in intensity between the light reflected from the bottom of the pits and the light reflected from the

Fig. 2. The position of the energy level with the lowest energy in the conduction band E_c and the energy level with the highest energy in the valence band E_v, showing the population of these bands near a pn junction (schematic). *a)* When there is thermal equilibrium between the conduction and valence bands the population of the energy states by electrons and holes can be indicated by a single Fermi level F. *b)* If a voltage is applied across the junction, the corresponding energy levels in the p-type and n-type material come closer together. The energy barrier is now so small that the charge carriers can cross the junction. The thermal equilibrium between the bands is now disturbed and the population of the bands can no longer be indicated by a single Fermi level. If the current that starts to flow through the junction is not too high, an equilibrium still exists in each separate band and the population of the levels can be represented as shown. This causes population inversion in a region around the pn junction and stimulated emission can occur.

surface of the disc. Because of interference, the light reflected by the bottoms of the pits is less intense than the light reflected by the surface of the disc. The detector signal therefore approximates to a rectangular waveform with two levels. In spite of precautions, some of the reflected light arrives at the output reflector of the laser (optical feedback) rather than the detector. This radiation can affect the laser action in the internal cavity, producing fluctuations in the intensity of the laser light. These fluctuations can be large enough to distort the intensity pattern of the light reflected from the disc, introducing read-out errors. To avoid these problems it is necessary to understand the mechanisms involved in this unwanted feedback.

This article describes our experimental and theoretical work on these problems. First we shall discuss the structure and characteristics of the laser without feedback. We shall then deal with the subject of optical feedback, making a distinction between coherent feedback and incoherent feedback. We make this distinction because the feedback radiation may not necessarily be coherent with the radiation in the laser cavity. If the feedback is coherent (at low feedback levels) a good theoretical description of the behaviour of the laser can be obtained. In this article we shall mainly confine ourselves to coherent feedback, with a brief mention of some of the effects encountered in incoherent feedback.

Laser structure

In the introduction we touched briefly on the principle of the semiconductor laser with a pn junction in a semiconducting material ('homojunction laser'). Structures of this type give laser action above a relatively high threshold current, which gives problems with overheating. Laser action can be obtained at a much lower current when the pn junction consists of two different semiconducting materials. For this reason lasers have been developed that consist of two layers of different composition [2], known as 'double-heterojunction lasers'. There are many structures and materials in use, depending on the characteristics required for a particular laser application. The structure of the laser we have used in our investigations is the one used in Compact Disc and LaserVision players. In
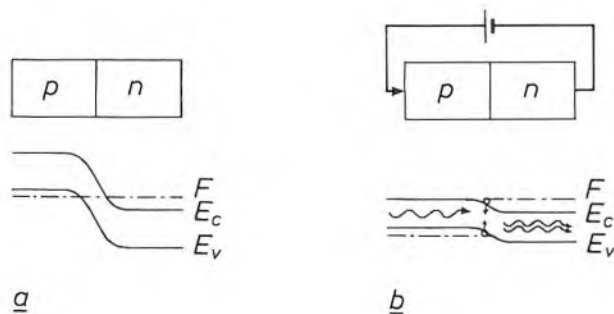
[1] Semiconductors can be either direct or indirect. The direct type is appropriate for laser action. This terminology indicates that the optical transitions between energy bands can take place directly, i.e. without the need for an extra impulse quantum of momentum, as required in indirect semiconductors.
[2] See J. C. J. Finck, H. J. M. van der Laak and J. T. Schrama, A semiconductor laser for information read-out, Philips Tech. Rev. 39, 37-47, 1980, and G. A. Acket, J. J. Daniele, W. Nijman, R. P. Tijburg and P. J. de Waard, Semiconductor lasers for optical communication, Philips Tech. Rev. 36, 190-200, 1976.

this section we shall take a brief look at the operation and characteristics of a laser with this structure. The problems that arise due to optical feedback are also to be found in many other laser structures, however. The results and the descriptions of these problems have a much wider relevance than for this special laser structure alone.

A cross-section through this structure is shown in *fig. 3*. The laser action is excited in layer A, the active layer, which consists of p-$Al_{0.14}Ga_{0.86}As$. This layer is sandwiched between two $Al_{0.45}Ga_{0.55}As$ layers, one p-type and the other n-type. (Since the Ga atoms in a GaAs lattice can be replaced by Al atoms without causing distortions or stresses in the lattice, it is relatively easy to make perfectly matching layers of different material.) Because of the difference in the aluminium content of the active layer and the boundary layers, the refractive index in the active layer is larger and the band gap is smaller than in the two adjacent layers. The band gap is the difference in energy between the lowest level of the conduction band and the highest level of the valence band. The energy-band diagram for this layer structure can be seen in *fig. 4*.

This structure of layers of semiconducting material is essentially that of an ordinary diode. When a voltage is applied across the diode in the forward direction the electrons of the n-type material and the holes of the p-type material move towards the active layer. Here both types of charge carriers are confined by the energy barriers ΔE_v and ΔE_c. Holes and electrons can only disappear from this active layer by radiative recombination (ΔE_v and ΔE_c are larger than the mean thermal energy of holes and electrons). Laser action in the diode starts when the current through the active layer is high enough to cause population inversion and the photons resulting from the radiative recombination can cause sufficient stimulated emission to compensate for the optical losses in the laser (the 'lasing' condition). To meet this condition the radiation has to be enclosed in a resonant cavity. This is effected in the y-direction by the difference in refractive index mentioned earlier. In the z-direction there is a step in the refractive index at the cleavage planes of the crystal, where about 30% of the radiation is reflected back into the laser cavity. The cavity boundary in the x-direction is formed by inserting a current-isolating layer of n-GaAs. The pnp structures on either side of the groove in this layer ensure that the current is limited to the groove, so that it is the only place where population inversion occurs. Since the laser light is present not only in the active layer but also in both boundary layers and even in a small zone of the current-isolating layer, there is a small step in the refractive index (5×10^{-3}) in the x-direction at the position
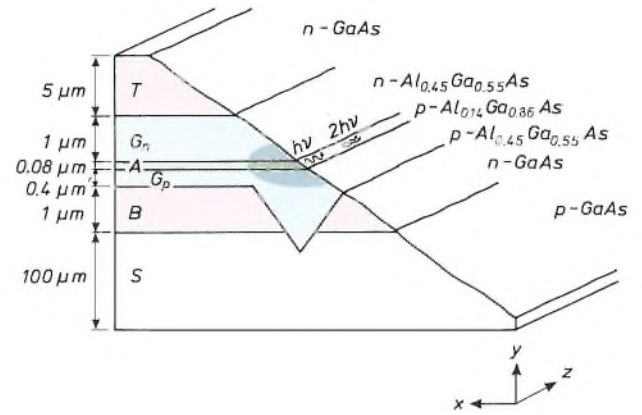
Fig. 3. Cross-section through the layer structure in a laser with a double heterojunction. A substrate S of p-GaAs contains, one above the other, a current-isolating layer B, a cladding layer G_p, an active layer A in which the laser action is produced, a cladding layer G_n and a top layer T, to which contacts can be applied. The V groove in the current-isolating layer ensures that the current injected into the structure in the y-direction is confined in the x-direction. Dimensions and compositions of the different layers are indicated in the figure. The laser light is generated in the grey area and propagates in the z-direction. The length of the layer structure in the z-direction is much greater than the transverse dimensions of the structure.
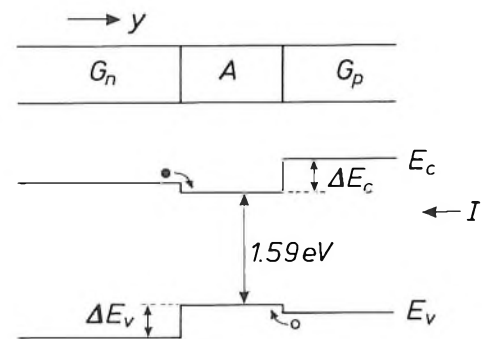
Fig. 4. Schematic representation of the band structure in the layers G_p, A and G_n of the laser. A current in the y-direction causes electrons in the conduction band of the n-type material to be pumped towards the active layer. Because of the energy difference ΔE_c between the conduction bands of the active layer and the boundary layer G_p, the electrons are confined. In an analogous way, holes collect in the active layer. Holes and electrons can only disappear from the active layer by recombination. Under the action of incident photons a coherent beam of radiation is thus produced.

of the V groove. As a consequence, light is optically confined in the x-direction as well.

The four layers are grown on a substrate of p-GaAs and this structure is then covered with a top layer of n-GaAs. These layers facilitate the application of contacts. As aluminium oxidizes easily, it is not easy to apply good metal contacts to AlGaAs.

A current in this structure in the y-direction produces radiation. *Fig. 5* shows the light output in the active layer as a function of the injection current. Up to a certain current value there is only spontaneous emission. The radiated power, the number of photons formed by recombination of electrons and holes, only
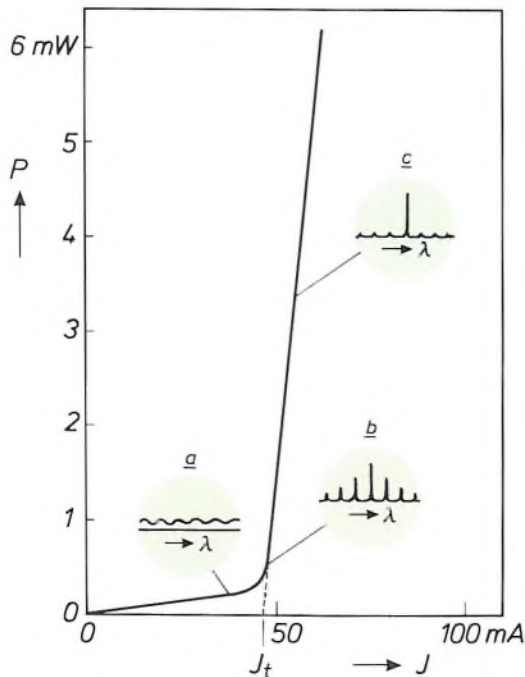
Fig. 5. Optical power P of the laser as a function of the current J. The spectrum of the laser is shown for a number of current values. *a*) Spontaneous-emission spectrum, *b*) multimode spectrum, *c*) single-mode spectrum.

increases slowly with the number of electrons injected into the active layer. When the injection current reaches a threshold value J_t, there is population inversion and stimulated emission can occur. Above this current the power increases strongly with current. At low currents the power is emitted in a fairly broad wavelength range (about 1 nm) close to 780 nm. When the current reaches a value well above the threshold current, the laser emits at a single sharply defined wavelength (single-mode behaviour with coherent radiation).

Optical feedback, experiments

In the applications of semiconductor lasers we have mentioned, the intensity or the laser power plays an important part, because it is the variation in the laser power reflected by the disc that contains the information to be read out or transmitted. This is why it is so important that the intensity of the laser is sufficiently constant for the intentional variations to be observed.

In a laser with no feedback there are various processes that cause fluctuations in the power. In the first place, there are small fluctuations in the laser power that are inherent in the process of radiative recombination (spontaneous emission). This noise contribution is fairly small and causes few problems, because it is constant above the threshold current. In addition, small changes in the input signal, the injection cur-

rent, affect the output signal or the laser power. Variations in the temperature of the laser structure also affect the laser power. It is therefore essential to keep the injection current and the temperature of the laser structure as constant as possible [3]. But even if all these conditions are satisfied, there may still be marked fluctuations in the laser power, if some of the laser radiation is reflected back into the internal cavity. This can happen to some extent when information is read from a Compact Disc or LaserVision disc and when a laser is connected to an optical fibre for communications purposes. Depending on the amount of radiation reflected back to the internal cavity and on the phase difference between the reflected radiation and the radiation in the laser, the optical field can become perturbed, giving large fluctuations of the laser power. We have studied this effect in the experimental arrangement described below (see *fig. 6*).

An image of the laser radiation (the 'spot') is formed by two lenses L_1 and L_2 on the feedback reflector M, which simulates a reflecting element such as a plate or the end of a fibre. The amount of feedback (the feedback fraction r) can be determined with the aid of filters located between the laser and the feedback reflector. The phase of the feedback radiation can be varied by moving the feedback reflector M and the lens L_2. A part of the laser beam is split off by a beam splitter B for measuring the spectrum, the power, the noise and the coherence of the laser radiation.

The output power and the spectrum of the laser depend on the current through the laser structure (see fig. 5). We shall have to take this current dependence
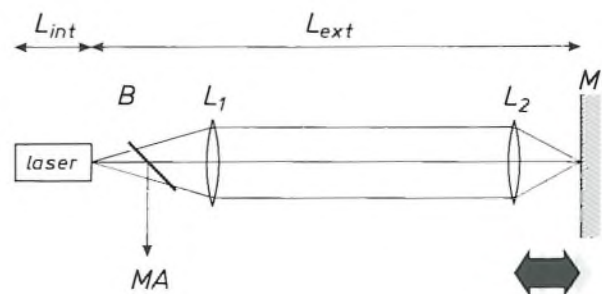
Fig. 6. Diagram of an experimental arrangement for determining fluctuations in the laser power. An image of the laser light is produced by two lenses L_1 and L_2 on the feedback reflector M. The feedback fraction can be varied with the aid of filters placed between the two lenses. The phase of the feedback radiation can be varied by moving the feedback reflector M and the lens L_2. A part of the laser beam is extracted through a beam splitter B for measuring the spectrum, the noise, the coherence, the wavelength and the power (MA).

[3] In our experiments we do indeed keep the temperature of the laser structure as constant as possible. In systems containing lasers a feedback loop with a photodiode controls the injection current of the laser to give constant output power.

into account if we want to study the fluctuations in the laser power as a function of the feedback parameters.

The laser power is measured with a P-I-N diode. The output signal of the diode is split to give a mean-value term ($<P>$) and a fluctuating term ($\Delta P(t)$). In the experimental arrangement the root-mean-square value of $\Delta P(t)$, $\sqrt{<(\Delta P(t))^2>}$, is determined in a band of about 3 kHz at a frequency of 200 kHz. The modulation index [4] m is defined as the ratio of this r.m.s. value to the mean value $<P>$. In *fig. 7* this modulation index is shown as a function of the current through the laser structure for a number of values of the feedback fraction. The phase of the feedback radiation is varied by moving the feedback reflector through a range of a few wavelengths. In this way minimum and maximum values for the modulation index are found. Fig. 7*a* shows the modulation index for a laser with no feedback. In general terms, the modulation index decreases with the injection current above the threshold value. (With no feedback the laser power, the d.c. component of the diode signal, increases while the fluctuations, the a.c. component of the diode signal, remain constant.) The abrupt change in the laser power at the threshold current appears here as a change in slope. Just above the threshold current there is a peak in the modulation index. It follows from wavelength measurements that this occurs at the current at which the laser ceases to emit at more than one wavelength (multimode behaviour) and starts to emit at a single wavelength (single-mode behaviour).
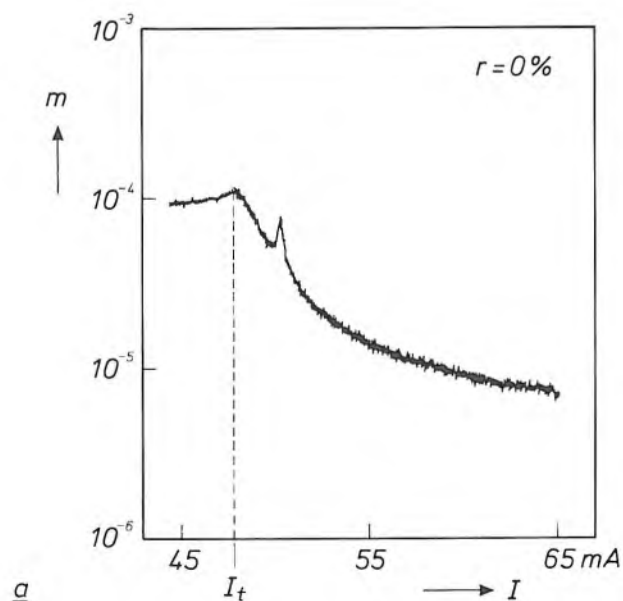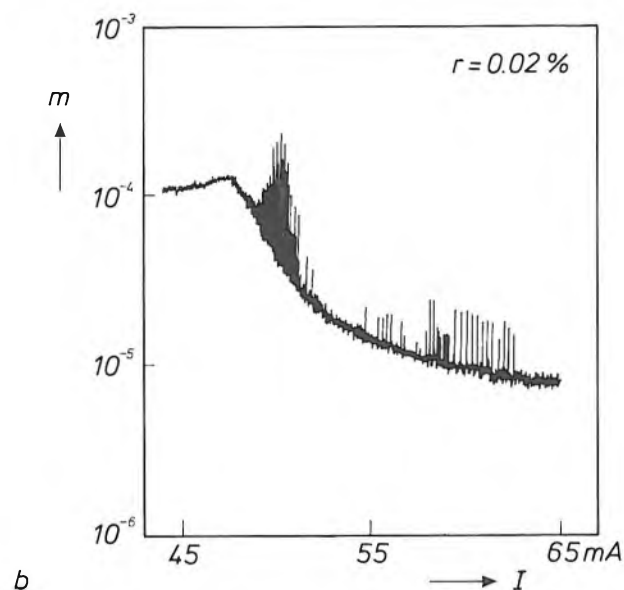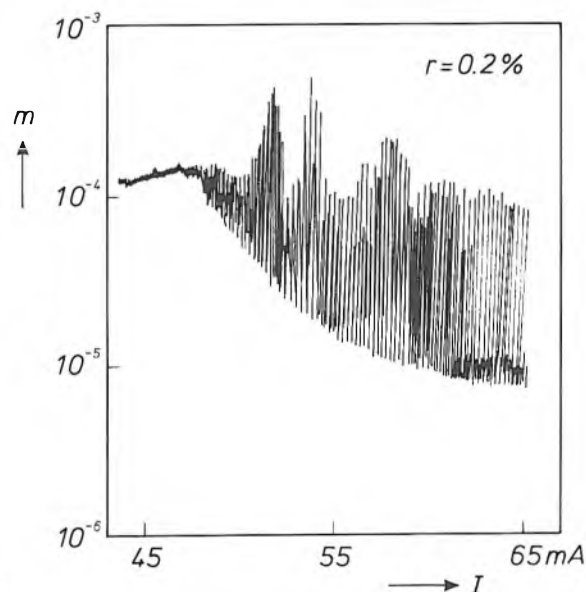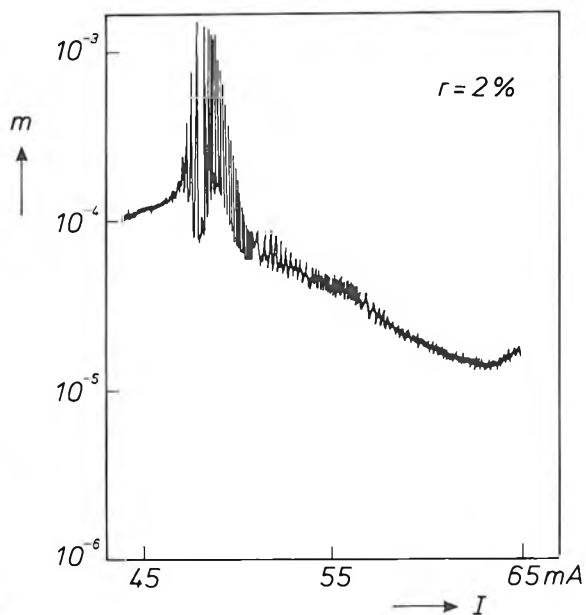
Fig. 7. The modulation index as a function of the injection current for different values of the feedback coefficient ($r = 0$, 0.02, 0.2 and 2%). In these measurements the length of the external cavity is varied through a range of a few wavelengths. In this way maximum and minimum values are found for the modulation index.

As feedback is increased (figs 7b to d) we see that the modulation index at this current value increases. Further above the threshold current the noise also increases with increasing feedback (figs 7b and c). Wavelength measurements show that the laser does not really operate in a single mode in these circumstances but that radiation at a single wavelength is alternated with radiation at other wavelengths. These are not the wavelengths determined by the length of the internal cavity. The separations between the possible wavelengths are in fact much less than the separations between the laser modes. The fluctuations in the intensity of the laser radiation arise because the laser jumps from mode to mode, and these fluctuations account for the higher modulation index.

At even higher feedback fractions ($r \approx 2\%$) the modulation index above the threshold current, although larger than with no feedback, is no longer so strongly phase-dependent. Wavelength measurements show that the laser spectrum has a number of stable modes. At this feedback value, however, there is a distinct increase in the noise near the threshold current. In the applications we are concerned with here, in which lasers are operated well above the threshold current, this contribution to the noise is not significant. In what follows we shall not therefore consider the threshold noise, and will take a closer look at the noise at low feedback levels, as can be seen in fig. 7b and c.

At a current above the threshold value the laser without feedback emits virtually monochromatic radiation. The wavelength of the radiation is one of the possible wavelengths determined by the length of the internal resonant cavity. The introduction of the feedback reflector has the effect of producing a second resonant cavity that also has a number of laser modes. The wavelengths of these modes are determined by the length of the external cavity and come between the wavelengths of the internal modes (see *fig. 8*). The presence of the external modes may cause laser light to be generated at a different wavelength from the wavelength corresponding to the internal mode. What happens depends on two factors, the amount of feedback and the difference in wavelength between an internal mode and the nearest external mode. Roughly speaking, as the feedback increases, the closer the ultimate wavelength becomes to one of the external modes. The wavelength difference between internal and external modes can be very precisely controlled by small variations in the position of the feedback reflector. With a symmetrical adjustment — i.e. with the internal mode exactly midway between two external modes — and sufficient feedback, the laser wavelength can go towards that of either of the modes. The
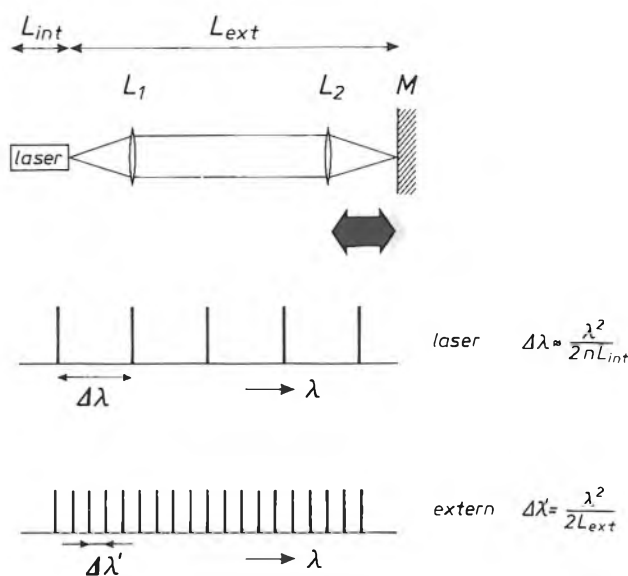

Fig. 8. Diagram showing the relative positions of the possible wavelengths of a laser with feedback. With no feedback the laser operates at one of the wavelengths indicated as laser modes. These wavelengths are fairly widely spaced. The effect of the feedback is that the wavelength at which the laser ultimately operates is a suitable compromise between a wavelength close to a laser mode and one that is close to an external mode.

actual 'choice' is not important here. We should note, however, that there is a particular feedback value at which the laser finds it hard to 'choose' between the two alternatives. The wavelength then oscillates at random between the two extremes, thus producing a great deal of noise.

Fig. 9 shows how the wavelength and power of the laser radiation change as a function of the phase of the feedback radiation, for three values of the feedback. The amount of radiation fed back is indicated by a dimensionless parameter C, which will be discussed later. If little radiation is fed back (fig. 9a) the variation in wavelength is small. If there is more feedback (fig. 9b) the effects are more pronounced. At even higher feedback values the laser wavelength may change so much that there is laser action on external modes (fig. 9c).

The effects that occur (corresponding to the results of fig. 9a, b or c) when there is feedback of laser radiation in the internal cavity are determined by the value of the feedback and the matching of the internal and external cavities (i.e. how close the external modes are to the wavelength of the laser without feedback).

[4] Determining the modulation index is a method of measuring the noise in a band of a particular bandwidth B. Another possible measure of the noise is the Relative Intensity Noise (*RIN*), which is the amount of noise per unit frequency, defined as $\langle \Delta P^2(v) \rangle / \langle P \rangle^2$. If the noise is white, i.e. independent of frequency, the relation between the two quantities is: $m = \sqrt{RIN \times B}$.
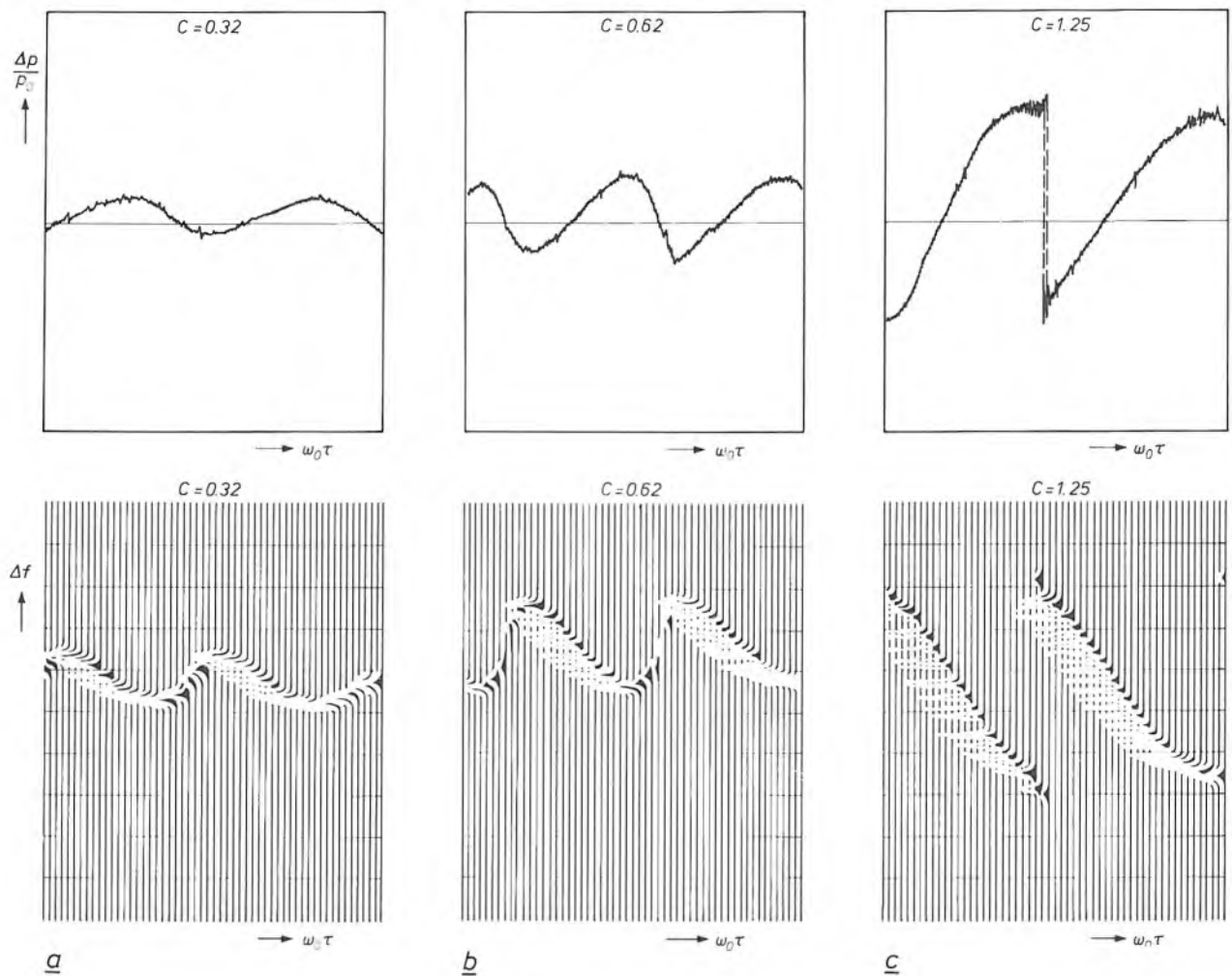
Fig. 9. The change in frequency (Δf) and the relative power change ($\Delta P/P_0$) of the laser radiation as a function of the phase ($\omega_0 \tau$) of the feedback radiation for three values of the feedback. The factor C takes account of both the feedback fraction and the matching between the external and internal laser cavities. As C increases the feedback increases. *a*) $C = 0.32$. *b*) $C = 0.62$. *c*) $C = 1.25$.

Both conditions can be described by a single parameter C, which takes account of the amount of feedback and the length of the external cavity. (It will be shown in the next section that there is a theoretical basis for the definition of such a parameter.)

The system parameter C contains the product of the feedback factor γ and the transit time τ of the radiation in the external cavity, and also a term connected with the change in the refractive index of the laser material because of the change in the concentration of charge carriers. The feedback factor is defined as:

$$\gamma = f \frac{c}{2l_{d,\,\text{eff}}} (1 - R) \sqrt{\frac{r}{R}}, \qquad (1)$$

where c is the velocity of light, $l_{d,\,\text{eff}}$ the effective length of the internal cavity, R the fraction of the radiation reflected by the laser reflectors in the internal cavity, r the fraction of the radiation reflected by the feedback reflector M, and f the fraction of the feedback radiation that actually arrives in the internal cavity of the laser.

It appears that there can be a maximum in the noise of the laser power for three values of this parameter (see *fig. 10*). The first maximum appears at $C \approx 1$. (This corresponds to a feedback fraction of only about 0.01% in the geometry of the arrangement used in fig. 8.) This maximum appears because the laser cannot choose between two symmetrical alternative wavelengths, as described above.

The second maximum appears because the laser jumps between more than two external laser modes ('mode hopping'). If the feedback is increased again there is also mode hopping between the internal laser modes (the third maximum). In this case the noise level is much higher than at lower feedback values because more modes are involved in the process. Finally, there is a stable situation in which the laser emits simultaneously at several wavelengths and a higher but constant noise level is present.
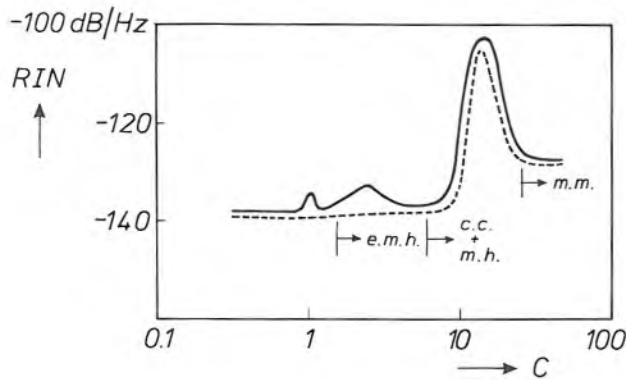
Fig. 10. The amount of noise [3] as a function of the parameter C (which takes account of the feedback and the matching between the external and internal cavities). Varying the phase of the feedback radiation gives a maximum value of the noise (continuous curve) and a minimum value (dashed curve). The figure also shows the regions where there is mode hopping between several external laser modes (e.m.h.), the regions where there is coherence collapse (c.c.), and the regions where there is mode hopping between laser-cavity modes (m.h.). Beyond the third maximum the laser gives a multimode spectrum.

In principle the effects that cause the noise peaks can be described in the same way. In all cases the noise arises as a result of mode hopping in the laser. In the situation where the second maximum appears, there are only external modes, whereas in the situation where the third maximum appears there are both internal and external modes.

In the next section we shall give a theoretical description of the first situation (corresponding to the appearance of the first maximum). It will be seen that the results calculated from this theory for the phase-dependence of the wavelength and the power agree with the experimental results.

The behaviour of the laser with high feedback is in reality more complicated than indicated above. The wavelength measurements show that in addition to the mode hopping of the laser between more than two wavelengths determined by the external and internal cavities, there is a marked broadening of the laser line. The linewidth, which amounts to a few tens of MHz at low feedback, increases to about 20 GHz. The coherence length of the laser (which is inversely proportional to the linewidth) has therefore decreased enormously (by a factor of 1000). We call this effect 'coherence collapse'. The feedback radiation is no longer coherent with the radiation produced in the internal cavity. Both the change in the linewidth, and the fact that the noise is independent of the length of the external cavity lead to the conclusion that the phase relation between the feedback radiation and the radiation in the internal cavity has been completely distorted. The parameter C has no further significance in this region, and strictly speaking the scale in fig. 10 ought to be replaced from $C = 5$ by a scale that only shows the feedback fraction.

Optical feedback, theory

Two important quantities for laser action in the active layer are the light intensity and the associated concentration of charge carriers. Statements about laser power and changes in it can be made if we know how these two quantities depend on the parameters of the laser cavity (refractive index, dimensions) and the current injected into the active layer. We shall examine the situation in a laser that emits monochromatic radiation, i.e. where the current in the active layer is greater than the threshold current.

The concentration of electron-hole pairs $n(t)$ in the active layer may change for three different reasons. In the first place the number of electron-hole pairs decreases as a result of spontaneous recombination. The number of electron-hole pairs that disappear per unit time in this way is inversely proportional to their mean lifetime T_1. The second process that causes electron-hole pairs to disappear is stimulated recombination. This number (of pairs that disappear in this way) is proportional to the intensity P of the radiation field in the active layer. Finally, electron-hole pairs are generated by the passage of a current through the active layer. The resulting change in concentration is J/qd, where J is the current, q the electronic charge and d the thickness of the active layer. Equation (2) expresses the change in concentration of electron-hole pairs due to all three processes:

$$\frac{dn(t)}{dt} = -\frac{n(t)}{T_1} - G_A(n(t))P + \frac{J}{qd}. \qquad (2)$$

The second term in this equation contains the intensity gain G_A, which in turn depends on the concentration of electron-hole pairs.

The change in the radiation field in the active layer can be described by considering the amplitude E of the optical field as a function of time. The light intensity in the cavity is equal to $|E|^2$. There are three contributions to the change in the field amplitude. The first is proportional to the gain $G_A(n(t))$, the second to the constant losses that arise because radiation leaks from the cavity, Γ_0, and the third is proportional to a dispersion factor $G_D(n(t))$ that takes account of the refractive-index variations due to variations in the concentration of electron-hole pairs. If there is any feedback radiation returning to the internal cavity after a time τ, the equation contains a further term that takes the feedback factor (γ) and the phase ($\omega_0\tau$) of this radiation into account. The equation for the change in the amplitude of the optical field is:

$$\frac{dE(t)}{dt} = \tfrac{1}{2}\left[G_A(n(t)) - \Gamma_0 + iG_D(n(t))\right]E(t)$$

$$+ \gamma E(t - \tau)e^{-i\omega_0\tau}. \qquad (3)$$

The factor $\tfrac{1}{2}$ appears in this equation because we are interested in the amplitude of the field here, whereas the expressions between brackets relate to the power.

The angular frequency of the laser with no feedback is ω_0. The quantity $\omega_0\tau$, which occurs in the exponent in (3), is the feedback phase referred to earlier. In this treatment we neglect multiple reflections. This is justified because the feedback factor γ is very small in the experiments that our model is intended to describe.

We assume that the system without feedback is in a stable state characterized by an intensity P_0, an electron-hole pair concentration n_0 and an angular frequency ω_0. We thus have:

$$G_A(n_0) = \Gamma_0, \; G_D(n_0) = 0 \text{ and } \frac{n_0}{T_1} = -\Gamma_0 P_0 + \frac{J}{qd}. \quad (4)$$

In a situation where there is feedback we can linearize the gain G_A and the dispersion G_D around n_0:

$$G_A(n) = \Gamma_0 + \xi(n - n_0), \quad G_D(n) = \eta(n - n_0). \quad (5)$$

This linearization permits us to express equations (2) and (3) that describe our model in terms of parameters that represent the situation with no feedback:

$$\frac{d}{dt}[n(t) - n_0] =$$

$$-\left(\frac{1}{T_1} + \xi P\right)[n(t) - n_0] - \Gamma_0[P(t) - P_0], \quad (6)$$

$$\frac{dE(t)}{dt} = \tfrac{1}{2}(\xi - i\eta)[n(t) - n_0]E(t) + \gamma E(t - \tau)e^{-i\omega_0\tau}. \quad (7)$$

We can thus describe the interaction between the optical field and the charge carriers by two interrelated differential equations, (6) and (7). If these can indeed describe our experimental results as discussed in the previous section, then they must permit single-frequency solutions that are stable under certain conditions. Closer examination [5] of our equations shows that such solutions do exist and that they are of the form $E(t) = \sqrt{P}\exp(i\Delta\omega t)$ and $n(t) = \overline{n}$ where P, $\overline{n}$ and $\Delta\omega$ are independent of time. The frequency shift $\Delta\omega$ resulting from the feedback, the power P and the concentration of charge carriers $\overline{n}$ are characterized by:

$$\Delta\omega\tau = C\sin[\phi_0 - (\omega_0 + \Delta\omega)\tau], \quad (8)$$

$$P = P_0 + 2\gamma\left(P_0 + \frac{1}{\xi T_1}\right)\frac{\cos(\omega_0 + \Delta\omega)\tau}{\Gamma_0 - 2\gamma\cos(\omega_0 + \Delta\omega)\tau}$$

$$\approx P_0 + \frac{2\gamma P_0}{\Gamma_0}\left(\frac{J/J_t}{J/J_t - 1}\cos(\omega_0 + \Delta\omega)\tau\right), \quad (9)$$

$$\overline{n} = n_0 - \frac{2\gamma}{\xi}\cos(\omega_0 + \Delta\omega)\tau. \quad (10)$$

The constant C ($= \gamma\tau/\cos\phi_0$, where $\tan\phi_0 = \eta/\xi$) in these solutions indicates the extent to which the intrinsic behaviour of the laser (frequency etc.) changes because of the feedback. We find in this parameter the feedback factor γ, the transit time τ of the radiation through the external cavity, and a quantity ϕ_0 that depends on the laser material and the structure of the laser. This justifies the introduction of the parameter C in the description of the experimental results (see page 297). We can compare the measured and theoretical behaviour of the frequency and power as a function of the phase of the feedback radiation if the equations (8), (9) can be solved for the quantities $\Delta\omega$ and P as a function of the phase $\omega_0\tau$. The power P has a cosine dependence on the phase of the feedback radiation (see eq. (9), subject also to the condition that the diode losses Γ_0 are much larger than the value of the feedback factor γ). A closer examination of the stability of the solutions shows that there are two different regions. If $C<1$, i.e. if there is little feedback, there is only one solution for $\Delta\omega$, but if $C>1$ there are more possibilities, which can be related to external modes.

In *fig. 11* the solutions of equations (8) and (9) are shown as $\Delta\omega\tau$ (a measure of the frequency shift) and $\cos(\Delta\omega + \omega_0)\tau$ (the power variation apart from a constant pre-factor) as a function of the phase $\omega_0\tau$ for a number of values of C. The continuous lines give the stable solutions and the dashed lines give the unstable solutions. In these calculations the ratio of the imaginary part to the real part of the refractive index, η/ξ, is equal to -4, a value close to the last known experimental value and characteristic of semiconductor lasers. This results in a value of $-76°$ for ϕ_0, so that $\Delta\omega$ and P are represented as a function of $\omega_0\tau$ by practically the same curves, but with opposite sign. Low values of C give a single stable solution ($C = 0.5$). If $C = 1$, both curves have a vertical slope at a particular value of the phase. At higher feedback levels ($C = 3$) there are three possible values for the power and the frequency shift in a particular phase range. As the phase goes through this range in both directions a hysteresis loop is described as indicated by the arrows. Laser action (stimulated emission) only occurs if the solution is stable. If small temperature and current fluctuations lead to an unstable solution, the laser jumps to the next stable solution. If C increases, more stable solutions become possible and the behaviour of the laser becomes more complicated.

We can determine the fluctuations in the power as a function of the phase by calculating the derivative of the power with respect to that phase. This is justified for the low-frequency fluctuations we are concerned with here (the frequency of the fluctuations in our ex-
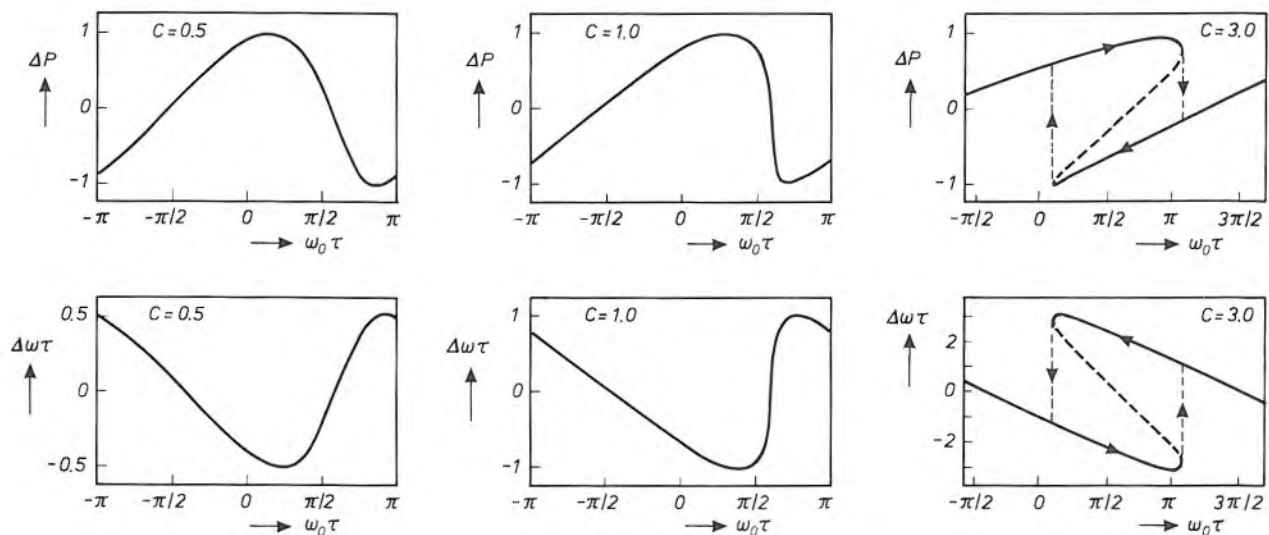
Fig. 11. The frequency shift $\Delta\omega\tau$ and the power P as a function of the phase $\omega_0\tau$ of the feedback radiation for different values of the parameter C.

periments is less than about 10^5 Hz. The calculation shows that most of the fluctuations will be in the neighbourhood of $C = 1$.

The calculated and measured results agree well. The feedback in the experiment can be calculated from a comparison of measured and calculated curves by determining C for the experimental curve. This is found to agree well with the feedback value as determined from the physical characteristics of the experimental arrangement (such as reflection coefficients of the laser and the feedback reflector and the length of the external cavity). It follows from the theoretical analysis that we can expect a large amount of noise in the vicinity of $C = 1$, which corresponds to the results of the experiments. The theory does not account for the large amount of noise indicated in fig. 10 for higher values of C; the parameter C cannot be used in the same way in this range since the linearization that we performed in equations (4) and (5) is no longer justified.

Tackling the noise problems

The good agreement found between the results of the experiments and the theoretical calculations indicate that we have gained a better understanding of the processes that are responsible for noise in the intensity of the laser radiation. But this does not mean that we have solved the problem introduced by this noise in the applications mentioned here. We can however indicate the conditions in which the operation of the laser will be least affected by noise. This is the case, for example, when the laser shows multimode behaviour (see fig. 10), which can arise in various ways. The noise level is then constant, although a little higher

than if there is no feedback. This can be taken into account by making the differences in intensity that contain the information substantially larger than this constant noise level.

In the first place, multimode behaviour of the laser can be obtained by providing high feedback. The effect of this is to reduce the threshold current and to increase the noise around the threshold (see fig. 7d). This presents no new problems because the lasers are operated well above the threshold current. Secondly, multimode behaviour can be induced by high-frequency modulation of the injection current. A third way of inducing multimode behaviour in the laser is to modify the structure of the laser. The laser we have described here is one whose characteristics are between those of a 'gain-guided' laser (with an optical gain profile), and an 'index-guided' laser (with a step in the refractive index). This implies that the laser cavity is partly formed by differences in the refractive index of the materials forming the layers of this structure. A laser of the gain-guided type, in which the cavity in the x-direction is defined by making only a restricted region suitable for the passage of current, gives multimode behaviour and therefore no noise problems arise. The threshold current of a gain-guided laser is higher, however, than in the laser structure discussed in this article. This higher threshold current introduces further problems connected with cooling and laser life. The beam quality of a gain-guided laser is also poorer because of astigma-

[5] More information about these calculations can be found in G. A. Acket, D. Lenstra, A. J. den Boef and B. H. Verbeek, The influence of feedback intensity on longitudinal mode properties and optical noise in index-guided semiconductor lasers, IEEE J. **QE-20**, 1163-1169, 1984.

tism. Consequently there is sufficient inducement in practice to use lasers with characteristics between those of the two types.

Another way of minimizing noise is to design a laser structure in which the system parameter C has the lowest possible value. Small values of C (<1) result in a low noise level; see fig. 10. The small value of C can be obtained, for example, by increasing the feedback of the laser reflectors (C is proportional to $1 - R$; see equation (1)).

In some applications noise is largely avoided by using lasers with reflectors that return nearly all the radiation into the internal cavity ($R \approx 1$), or lasers that are forced into multimode behaviour by modulation of the injection current.

Summary. Fluctuations in the optical power of semiconductor lasers can arise because of radiation returning to the laser cavity after reflection from a surface outside the cavity. These fluctuations are undesirable in many applications in which information is optically transmitted as variations in laser power. Experiments and calculations have been carried out to gain a better understanding of the ways in which these fluctuations are affected by the various laser parameters. Experimental and theoretical results agree well. Conditions can now be indicated in which there is very little variation in laser power as a result of feedback of optical power.

1937   THEN AND NOW   1987

Permanent magnets
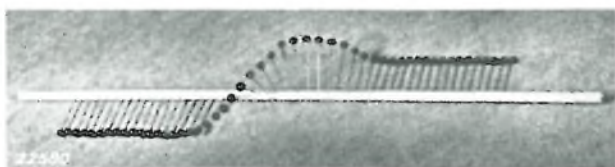
Although permanent magnets have been used for many centuries — in the compass — a good model for explaining ferromagnetic behaviour has only been available since the beginning of the twentieth century. This was when it was first understood that magnetic material consists of small domains of magnetic moments all pointing in the same direction, and that the domains could change their orientation by the movement of a 'Bloch wall' (see the illustration [*] at the top left). With a better understanding of magnetism, it became possible to control the microstructure of alloys and oxides of the ferromagnetic elements — iron, cobalt, nickel — so that their $(BH)_{max}$-values were ten or twenty times those of the classic magnet steels. 'Ticonal G' from 1937, 'Ferroxdure II' from 1954 and 'Ticonal XX' from 1956 were all results of such work at Philips on the perfection of magnetic materials (see the two electron micrographs on the right, taken in perpendicular directions in 'Ticonal XX').

Later on, elements from the rare-earth group were applied, as well as the traditional ferromagnetic elements. This led to the discovery of $SmCo_5$ in 1968 and $Nd_2Fe_{14}B$ in 1983. Philips are about to apply the latter material in the pick-up of the CD player.

A striking picture of the progress during the last twenty or thirty years is obtained by comparing the load (the brass rods, colour photo) that the various kinds of magnets, of the same dimensions, can support if they levitate at the same distance above an 'opposite pole'.

'Ticonal' does not appear in this picture, since its best features, the combination of a high saturation magnetization and a small coercivity (just the opposite of 'Ferroxdure', which has a low saturation magnetization and a high coercivity), do not show to their best advantage in such an experiment.
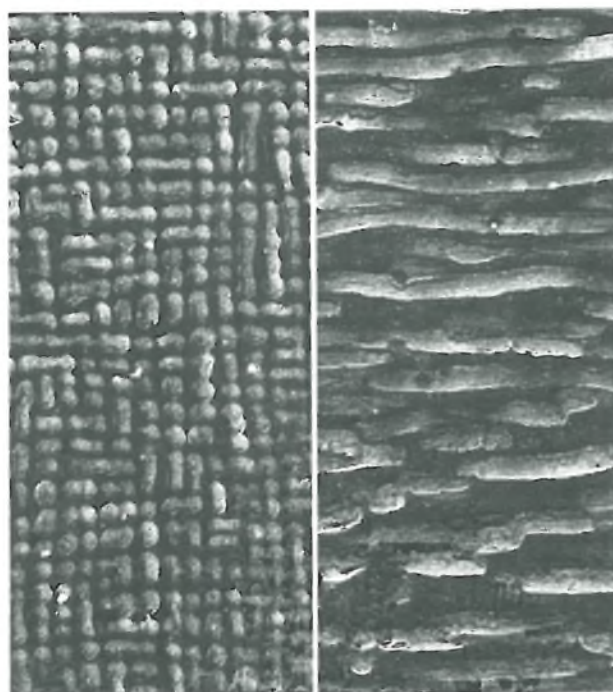
[*] From Philips Technical Review, August 1937.

Metastable phases and thermodynamic equilibrium

J. J. van den Broek and A. G. Dirks

The hardening of steel is one of the oldest and best-known processes in which a metastable crystalline phase occurs. A supersaturated solution of carbon in iron is formed, and the associated crystalline structure is called martensite. Metastable amorphous phases in metal alloys have been the subject of keen interest in recent years because of their interesting properties, which arise because they have no regular atomic order and no grain boundaries. The occurrence of metastable phases, either amorphous or crystalline, can in many cases be predicted from the tendency of every system to seek a minimum of the Gibbs free energy. For predictions of this kind the familiar phase diagram, which applies to a state of stable equilibrium, can be a valuable aid.

Introduction

Until about 1934, when amorphous metal was first successfully produced from the vapour phase, only the crystalline form of metals was known. Technical applications of amorphous metal did not emerge until the seventies, when it became possible to produce this material in the form of a metallic ribbon. The method consisted in rapidly cooling metal in the liquid state by squirting it on to a copper wheel rotating at high speed. It seemed likely that the absence of preferred directions for the magnetic moment would give metals with better magnetic properties, and that the absence of grain boundaries would yield metals of much greater strength [1].

Amorphous metals have not yet become as widely applied as first seemed likely. In the past fifteen years, however, there has been renewed interest. This is partly due to the emergence of a new application in the form of thin films for magneto-optical recording [2]. These films are made by evaporating the components on to a cooled substrate, so that atomic disorder is 'frozen in' [3]. Another innovation has been the introduction of mechanical alloying, which can be used, it appears, to permit the economical use of amorphous metal for exceptionally strong mechanical compo-

Ir J. J. van den Broek and Dr A. G. Dirks are with Philips Research Laboratories, Eindhoven

nents. In this method the constituents are ground to a fine powder and then intimately mixed [4]. An industrial application announced recently is the use of amorphous metal ribbon in transformer cores. The losses are lower, so that energy can be saved and the transformers can be much smaller.

Amorphous metals are always metastable, which means that a fairly significant disturbance, such as a sudden increase in temperature, can make the metal become crystalline. Evaporation from the vapour phase can produce both metastable *amorphous* alloys and metastable *crystalline* alloys. We have even been able to make homogeneous mixtures of metals that are normally so immiscible that two phases occur both in the solid state and even in the liquid state (like oil in water) [5].

According to the laws of thermodynamics a system at constant temperature and pressure tends towards an equilibrium state with a minimum of the Gibbs free energy [6]. The Gibbs free energy G is defined as:

$$G = U - TS + pV, \tag{1}$$

where U is the internal energy, T the absolute temperature, S the entropy, p the pressure and V the volume. The quantity $U + pV$ is called the enthalpy (H). In all

known metal alloys at room temperature the Gibbs free energy of the amorphous phase is greater than that of the most stable crystalline phase, i.e. the phase with the lowest Gibbs free energy. This explains why an amorphous phase is always metastable. If the mobility of the atoms at room temperature is insufficient to cause the amorphous structure to become crystalline, the amorphous structure can maintain itself.

The phase diagram, an invaluable aid in phase theory, shows the phases that occur at different temperatures and compositions (fractions) of the components. These phases are the various crystalline phases, the liquid phase or phases and sometimes the gas phase. The phase diagram is directly related to the (G, x) diagram, which gives the Gibbs free energy G at a given temperature for the various phases as a function of the mole fraction x [7]. N. Saunders and A.P. Miodownik have also pointed out that the (G, x) diagram can often be used for predicting whether metastable phases will occur [8], especially for alloys that have been made by depositing the components on to a cold substrate from the vapour phase. The mobility of the atoms is then usually so low that the homogeneous distribution due to the evaporation remains unchanged. At a particular composition the phase obtained is the one that has the lowest Gibbs free energy, provided that the crystal structure is not too complicated to form on the cold substrate. As a rule, then, two separate phases do not occur, although this often happens when a state of stable equilibrium is reached.

The difficulty with predicting metastable amorphous and crystalline phases from the (G, x) diagram is that for most combinations of metals the diagram is not known and is also difficult to calculate [9]. A method of approximation for predicting amorphous phases, which requires no calculations, is known from phase theory [7]. In this method the location of a composition region where amorphous alloys may occur is given by extrapolating liquidus curves in the phase diagram. If the phase diagram of an alloy system is known, this method soon gives a result, and is just as useful for making predictions as the (G,x) diagram.

In the rest of the article we shall first consider the phase diagram and its relation to the (G, x) diagram. We shall then show how metastable phases can be predicted with the (G, x) diagram. Next, we shall deal with the prediction of amorphous phases with the aid of the phase diagram. Both methods will be illustrated by practical examples. Finally we shall look at the complicated phase relationships that can arise in a transition region between a state of stable thermodynamic equilibrium and a state of metastable equilibrium.

The phase diagram and its relation to the (G, x) diagram

First of all we shall recall the basic principles of the phase diagram. *Fig. 1* shows a (G, x) diagram and the phase diagram for two metals A and B that are completely soluble in each other in the liquid and solid states [7], e.g. silver and gold. (The mole fraction x is the ratio of the number of atoms B to the total number of atoms in the mixture.) The complete mutual solubility is connected with the identical crystal structures of pure gold and silver and the virtually identical atomic radii of both elements. In mixed crystals silver and gold atoms can therefore be substituted for one another in any mixing ratio.

The shape of the curves in the (G, x) diagram for the various phases depends on the temperature T, since

[1] J. Kramer, Über nichtleitende Metallmodifikationen, Ann. Phys. 19, 37-64, 1934;
R. Hilsch, Amorphous layers and their physical properties, in: V. D. Frêchette (ed.), Non-crystalline solids, Wiley, New York 1960, pp. 348-373;
F. E. Luborsky (ed.), Amorphous metallic alloys, Butterworths, London 1983;
P. Duwez, Structure and properties of alloys rapidly quenched from the liquid state, Trans. Metall. Soc. 60, 607-633, 1967;
K. H. J. Buschow, Research on amorphous alloys, Philips Tech. Rev. 42, 48-57, 1985.

[2] J. W. M. Biesterbos, Properties of amorphous rare earthtransition metal thin films relevant to thermomagnetic recording, J. Physique 40 (Colloque C5), C5/274-C5/279, 1979;
M. Hartmann, B. A. J. Jacobs and J. J. M. Braat, Erasable magneto-optical recording, Philips Tech. Rev. 42, 37-47, 1985.

[3] S. Mader, Metastable alloy films, J. Vac. Sci. & Technol. 2, 35-41, 1965.

[4] R. B. Schwarz and W. L. Johnson, Formation of an amorphous alloy by solid-state reaction of the pure polycrystalline metals, Phys. Rev. Lett. 51, 415-418, 1983;
E. Hellstern and L. Schultz, Amorphization of transition metal Zr alloys by mechanical alloying, Appl. Phys. Lett. 48, 124-126, 1986;
A. W. Weeber, K. van der Meer, H. Bakker, F. R. de Boer, B. J. Thijsse and J. F. Jongste, The preparation of amorphous Ni-Zr powder by mechanical alloying, J. Phys. F 16, 1897-1904, 1986.

[5] A. G. Dirks and J. J. van den Broek, Metastable solid solutions in vapor deposited Cu-Cr, Cu-Mo, and Cu-W thin films, J. Vac. Sci. & Technol. A 3, 2618-2622, 1985;
J. J. van den Broek, A. G. Dirks and J. L. C. Daams, Phase relationships in binary alloy thin films, Proc. Int. Symp. Trends and New Applications in Thin Films, Strasbourg 1987, pp. 421-425.

[6] J. D. Fast, Entropy in science and technology, Philips Tech. Rev. 16, 258-269 and 298-308, 1955.

[7] J. L. Meijering, Phase theory, Philips Tech. Rev. 26, 12-26 and 52-60, 1965.

[8] N. Saunders and A. P. Miodownik, The use of free energy vs composition curves in the prediction of phase formation in codeposited alloy thin films, CALPHAD 9, 283-290, 1985;
N. Saunders and A. P. Miodownik, Thermodynamic aspects of amorphous phase formation, J. Mater. Res. 1, 38-46, 1986.

[9] The enthalpy H can be calculated with the aid of A. R. Miedema's models. Since the term TS in eq. (1) for the Gibbs free energy is small at room temperature, these models can sometimes be used for determining the Gibbs free energy.
See: A. R. Miedema, The atom as a metallurgical building block, Philips Tech. Rev. 38, 257-268, 1978/79;
A. K. Niessen and A. R. Miedema, The enthalpy effect on forming diluted solid solutions of two 4d and 5d transition metals, Ber. Bunsenges. Phys. Chem. 87, 717-725, 1983;
A. R. Miedema, P. F. de Châtel and F. R. de Boer, Cohesion in alloys — fundamentals of a semi-empirical model, Physica 100B, 1-28, 1980.
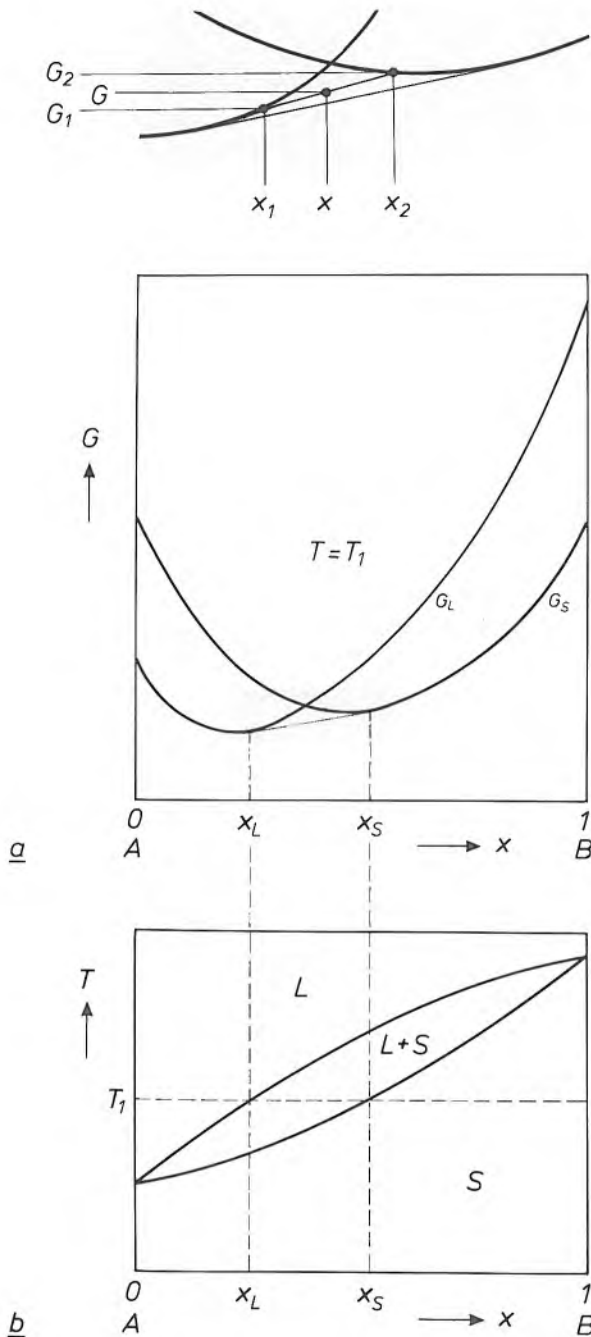
Fig. 1. Principles of the phase diagram. *a)* A (G,x) diagram, the Gibbs free energy G as a function of the mole fraction x of B in the mixture of A and B, at a temperature $T=T_1$, G_L Gibbs free energy of the liquid phase L. G_S the same, for the solid phase S. x_L and x_S boundaries of the composition range where, in stable equilibrium, there are two phases, the liquid phase and the solid phase. In this range the Gibbs free energy for a given mole fraction follows from the common tangent of the (G,x) curves. The enlarged diagram at the top shows that the Gibbs free energy G of a mixture of two phases (G_1,x_1) and (G_2,x_2) at a fraction x follows from the line connecting the corresponding points. In a state of stable equilibrium the appropriate combinations of G and x lie on the common tangent. *b)* The phase diagram for two elements that are completely soluble in each other both in the liquid state and the solid state. The corresponding (G,x) diagram shown in (*a*) applies at a temperature T_1. The phase diagram can be thought of as being formed from a number of (G,x) diagrams at different temperatures. The region $L+S$ is two-phase.

the Gibbs free energy G is a function of temperature, of course; see eq. (1). Fig. 1*a* shows the (G,x) diagram for a temperature T_1 higher than the melting point of pure A and lower than that of pure B. At this temperature, A with little B is liquid, B with little A is solid. To the left of the point where the curves intersect, the liquid phase has a lower Gibbs free energy than the solid phase. The liquid phase is therefore more stable here. On the right the same is true for the solid phase. In a state of stable equilibrium there is a composition region near the intersection point of the two (G,x) curves where the solid and the liquid phases form a two-phase mixture. The boundaries x_L and x_S of this range follow from the location of the points of contact with the common tangent. In stable equilibrium the Gibbs free energy of the two-phase mixture is determined by the point on the common tangent that corresponds to the mole fraction x of the alloy under consideration.

It can be seen from the inset in fig. 1*a* that the common tangent of the (G,x) curves must be drawn to find the Gibbs free energy of a mixture in the range $x_L < x < x_S$. Suppose that at a fraction x a liquid phase forms with Gibbs free energy G_1 and fraction x_1 and a solid phase with G_2 and x_2. The Gibbs free energy of the mixture of liquid and solid is then found for the fraction x by drawing a straight line between the points (x_1,G_1) and (x_2,G_2)[7]. The Gibbs free energy of the two-phase mixture is lower than that of homogeneous liquid or homogeneous solid solutions of the same composition. However, of all the possible lines that connect points on the curves, the common tangent to the curves at the fractions x_L and x_S represents the lowest Gibbs free energy that is possible for intermediate fractions.

The stable equilibrium at a temperature T_1 can be described as follows; see fig. 1*a*. Mixtures that are rich in A are liquid when $x < x_L$. Mixtures that are rich in B are solid when $x > x_S$. Mixtures with $x_L < x < x_S$ consist both of a liquid of mole fraction x_L and of single-phase solid solution of mole fraction x_S. According to the 'lever' rule, the amount of solid solution varies from 0% at $x=x_L$ to 100% at $x=x_S$.

The phase diagram corresponding to the system A-B in fig. 1*a* is shown in fig. 1*b*. There is a region, indicated as $L+S$, in which the liquid and the solid phases coexist. The boundaries of this region are given by the contact points of the common tangents of pairs of curves in (G,x) diagrams at different temperatures, as demonstrated for the temperature T_1. In region S there is a single phase of solid solutions which, unlike pure A or pure B, do not have a melting point but a melting range. The phase diagram describes a state of stable thermodynamic equilibrium.

Fig. 2 gives a (G, x) diagram and the phase diagram for a multiple eutectic system A-B in which compounds A_2B and AB_2 occur. The structures α, β, γ, and δ of pure A, pure B, and the two compounds respectively are different, so that at low temperatures only phases of nearly pure A, nearly pure B or a compound occur. In the (G, x) diagram, which corresponds here to a temperature (T_2) with solid phases only, curves are shown for the Gibbs free energies G_α, G_β, G_γ and G_δ. Here again, the common tangents of the (G, x) curves are shown, resulting in three broad two-phase regions in the phase diagram. Crystal structures of the compounds A_2B and AB_2 only form at the virtually fixed ratios A/B of 2 and 1/2, at which the atoms A and B occupy fixed places in the crystal structures. Examples of systems with compounds are copper-zinc, samarium-cobalt and nickel-zirconium. We shall return to the system nickel-zirconium presently.
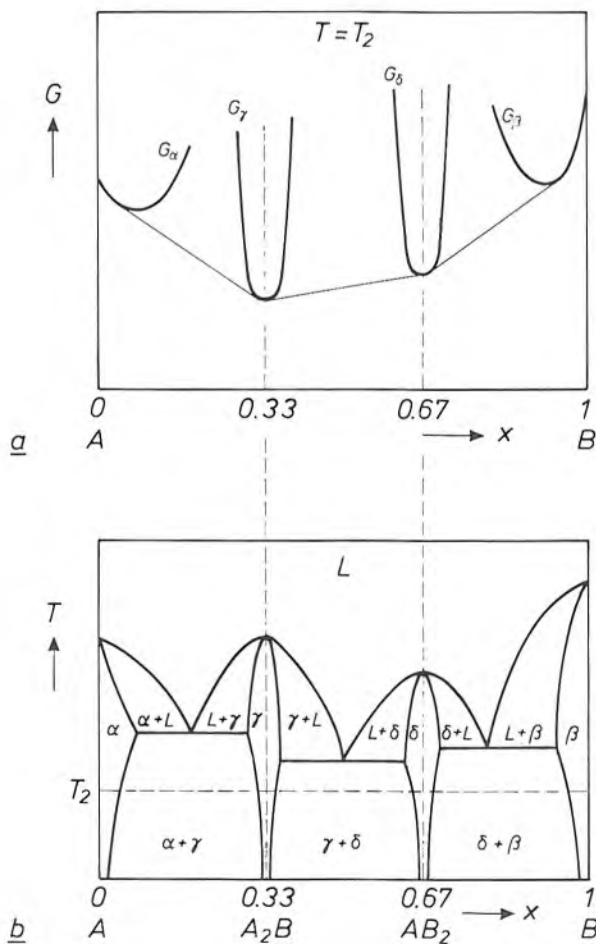

a

b

Fig. 2. *a*) A (G, x) diagram and *b*) the phase diagram for a multiple eutectic system A-B with compounds A_2B and AB_2. The crystal structures of pure A and B are indicated as α and β, and those of the compounds as γ and δ. G_α, G_β, G_γ and G_δ are the Gibbs free energies of the various structures. The (G, x) diagram relates to a temperature T_2. $\alpha + \gamma$, $\gamma + \delta$, $\delta + \beta$, $\alpha + L$, $L + \gamma$, $\gamma + L$, etc. are two-phase regions. *L* liquid phase.

Predicting metastable phases with the aid of the (G, x) diagram

In determining two-phase regions with the aid of the common tangent of (G, x) curves it is assumed that the atoms possess so much mobility that the two phases with different structures and mixing ratios are in fact formed. After rapid cooling from the liquid phase or deposition from the vapour phase (we shall use the term 'quenching' for both processes) this mobility is sometimes so small, however, that the separate phases cannot form. In such cases, therefore, there is no point in drawing the common tangent. Saunders and Miodownik have pointed out that instead of two separate phases a single phase occurs, which is usually the phase that, according to the (G, x) diagram, has the smallest Gibbs free energy [8].

This is illustrated in *fig. 3*. For the system A-B the (G, x) diagram in fig. 3*a* shows curves for the crystal structures α, β and γ. Fig. 3*b* shows the phases that are formed in a state of stable equilibrium. On either side of the two-phase region $\alpha + \beta$ there are single-phase regions α and β. The structure γ is not formed, because the (G, x) curve lies above the common tangent of the curves for G_α and G_β. Fig. 3*c* applies to a situation after quenching. The boundary of the regions α and β is defined by the point where the corresponding curves in fig. 3*a* intersect. It is assumed that no phase γ is formed; this may be the case if it is difficult for crystallization nuclei to form or if the crystallization nuclei grow too slowly, e.g. because the structure is too complicated. If the phase γ does form, we have the situation shown in fig. 3*d*. There are then three single-phase regions, whose boundaries are given by two intersection points in fig. 3*a*.

The probability that a third metastable phase, either crystalline or amorphous, will be formed in addition to α and β increases with the area of the grey-shaded region in fig. 3*a* between the two curves and their common tangent. This area is large, for example, when element B does not 'fit' so well into the structure α of element A, since the difference $G_\alpha{}^B$-$G_\beta{}^B$ will then be greater. This is the thermodynamic background to the 'structural difference rule'[10].

We can illustrate the theory above with data from Saunders and Miodownik [8]. *Fig. 4a* shows how the composition range for an amorphous phase is determined for the nickel-zirconium system. The continuous curves give the Gibbs free energy G at room temperature as a function of the fraction x for different

[10] B. X. Liu, Ion mixing and metallic alloy phase formation, Phys. Stat. Sol. A 94, 11-34, 1986.

crystalline phases and for the liquid phase. The small squares relate to the amorphous material. It can be seen that there is a relatively large difference between the Gibbs free energy of the amorphous phase and that of the liquid phase. This is a little surprising, since the usual assumption is that they are just about equal. The difference is probably a consequence of some short-range ordering of the atoms in the amorphous phase. The points marked + indicate the minimum Gibbs free energy for different compounds of Ni and Zr; see the phase diagram in fig. 4b [11]. The atoms do not have sufficient mobility for these compounds to be formed, however, so that we can disregard these points. The range where the amorphous phase would
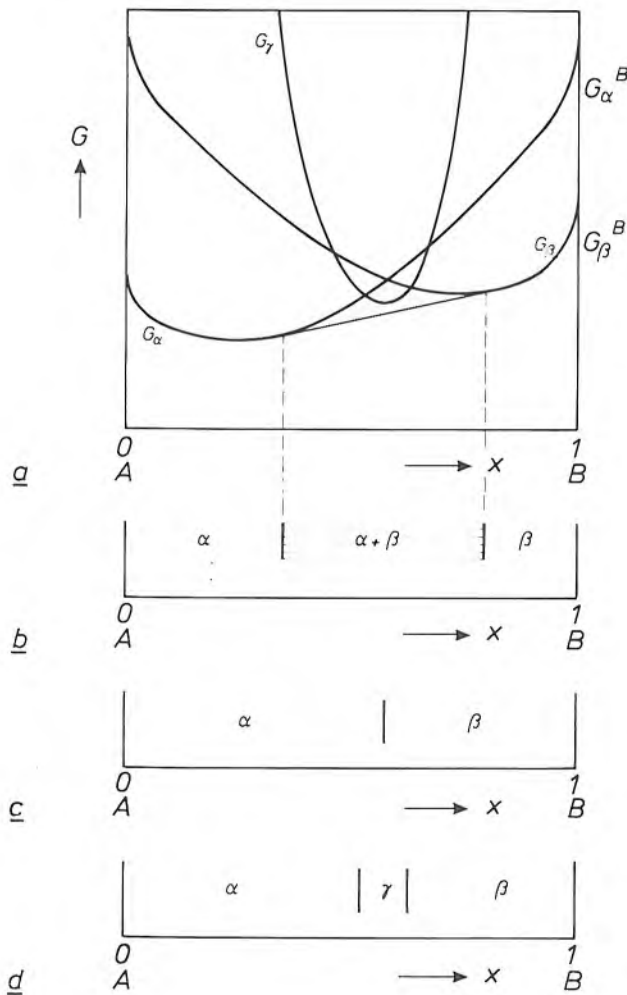
be expected follows from the points where the curve for this phase intersects that for the face-centred cubic structure.

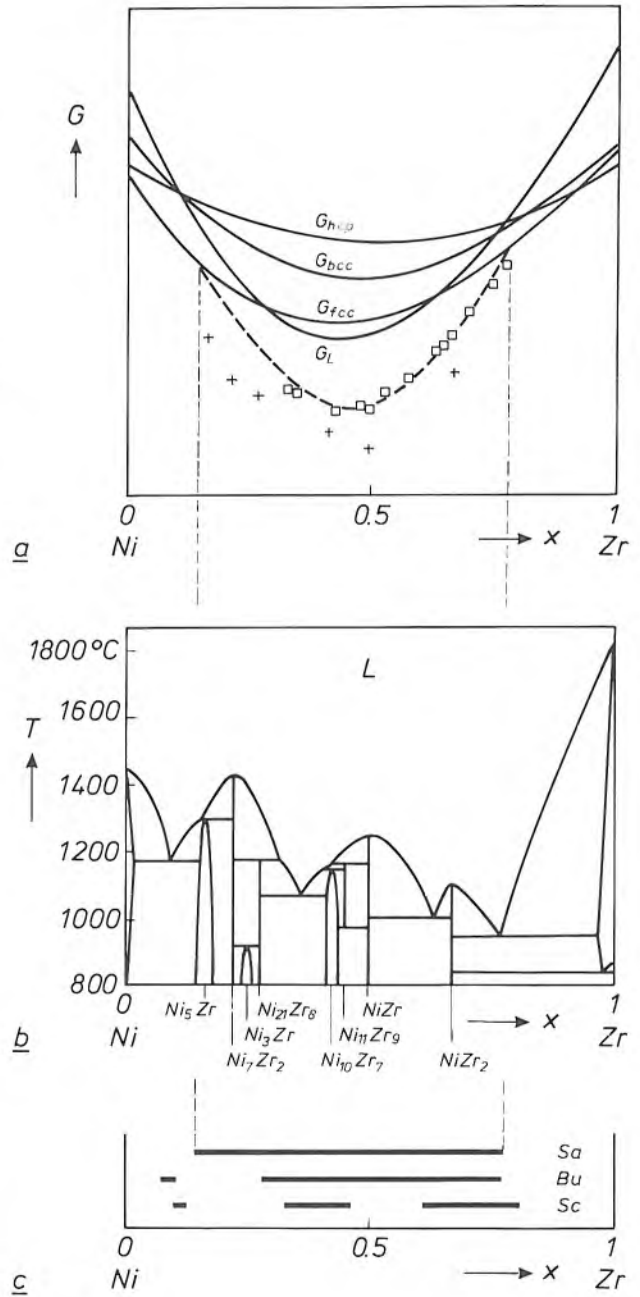Fig. 4c shows the very broad amorphous range (Sa) found in this way, together with the results of experi-

Fig. 3. a) (G, x) diagram at room temperature for the system A-B with phases α, β and γ. G_α^B and G_β^B Gibbs free energy of B with the respective structures β and α. b) The phases at room temperature in a state of stable equilibrium as a function of the different mole fractions x. The single-phase composition ranges are indicated. The two-phase range, whose location follows from the common tangent in (a), is shown by horizontal hatching. c) The same situation, but now for 'quenching' from high temperature. There are now only two single-phase composition ranges, whose separation is given by the intersection point of the curves for α and β in (a). It is assumed that the structure γ does not form, for example because it is too complicated. d) The situation if the structure γ actually did form.

Fig. 4. a) The (G, x) diagram [8] at 25 °C, and b) the phase diagram [11] for the system Ni-Zr. hcp hexagonal close-packed structure. bcc body-centred cubic structure. fcc face-centred cubic structure. G_{hcp}, G_{bcc}, G_{fcc} and G_L Gibbs free energy of these structures and of the liquid phase. The points indicated by squares relate to amorphous material. The points marked by + are the minima of (G, x) curves not shown (see fig. 2a) for the various compounds indicated in (b). c) Composition ranges in which amorphous material can be found after quenching. Sa the (theoretical) range that is given by the points in (a) where the curve for amorphous material intersects the curve for the fcc structure. Bu the range found experimentally by Buschow [12]. Sc the range found experimentally by Scott [13].

ments. The ranges *Bu* were found at our Laboratories by K. H. J. Buschow; they are the result of quenching from the liquid phase on a rapidly rotating wheel [12]. The ranges *Sc*, found by M. G. Scott and presented in a review article by H. A. Davies, are also the result of quenching from the liquid phase, but with a different technique [13]. The agreement between the theoretically predicted range and the results of experiments is satisfactory. It should be remembered here that high accuracy cannot be expected in predictions of this kind, since the (G, x) curves are no more than approximations and because the cooling rate during quenching determines the phases that are actually formed. We shall return to this point later.

The method described can also be used for predicting metastable crystalline phases as well as amorphous phases [8]. We shall illustrate this with the copper-chromium, copper-molybdenum and copper-tungsten systems, which we have investigated. These metals have such poor miscibility in one another that two phases are formed even in the liquid state. We have also investigated the copper-cobalt system; these metals only have poor miscibility in the solid state [5]. On a substrate at room temperature we deposited thin films of these metal alloys from the vapour phase in different proportions and found broad — metastable — single-phase regions that were separated by fairly narrow two-phase regions, as shown in *fig. 5*. (If the substrate had been cooled well below room temperature, these two-phase regions would have been even narrower, giving the situation illustrated in fig. 3c.) In a state of stable equilibrium, i.e. not after quenching, these alloys always consist of two phases for all compositions, the two phases being the pure metals.

The location of the two-phase regions that form the limits of the single-phase regions should again follow from the intersection points of the (G, x) curves. Since these curves are not known in this case, we had to determine the location of the intersection point in a complicated and rather roundabout way. We plotted the energy of formation instead of the Gibbs free energy as a function of the mole fraction x. The energy of formation is the part of the Gibbs free energy that is necessary to make the metals alloy. The only contribution to the energy of formation we took into ac-

count was ΔG_{latt}, which is a measure of the stability of the metal in the crystal lattice [14]. The energy required for the physical mixing is practically independent of the crystal structure and was not therefore
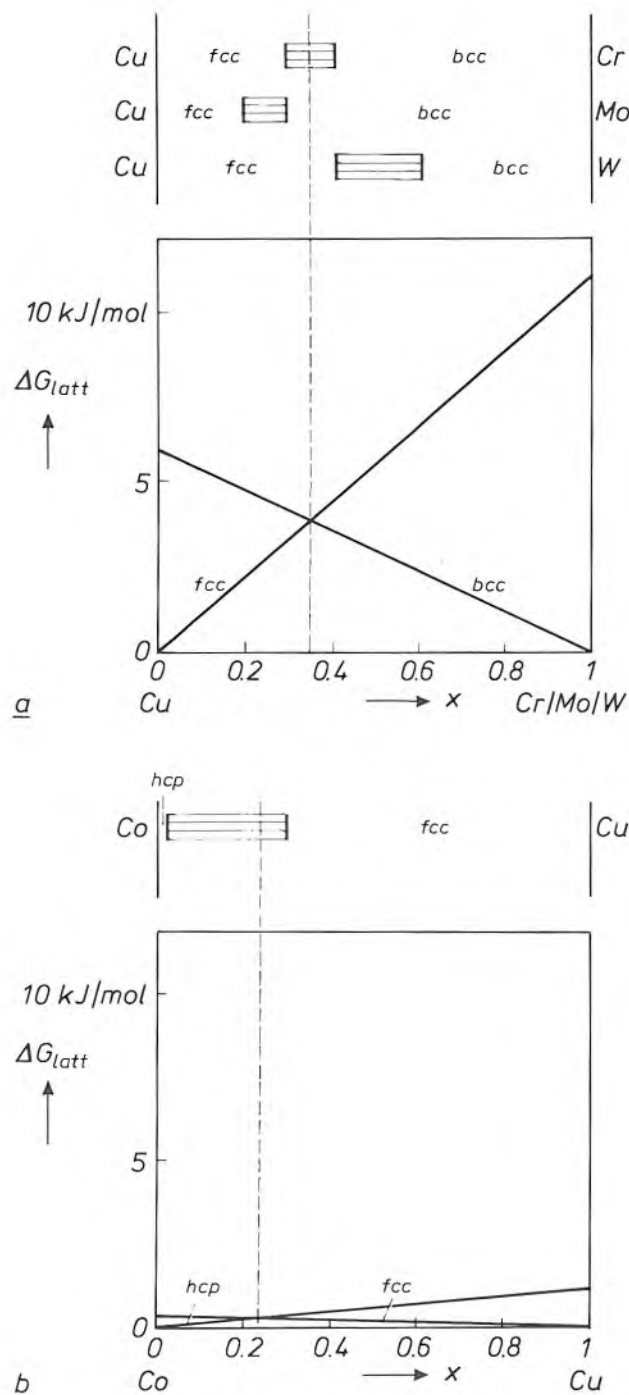
[11] P. Nash and C. S. Jayanth, The Ni-Zr (nickel-zirconium) system, Bull. Alloy Phase Diagrams 5, 144-148, 1984.
[12] K. H. J. Buschow, Short-range order and thermal stability in amorphous alloys, J. Phys. F 14, 593-607, 1984.
[13] H. A. Davies, Metallic glass formation, in: F. E. Luborsky (ed.), Amorphous metallic alloys, Butterworths, London 1983, pp. 8-25.
[14] See: L. Kaufman and H. Bernstein, Computer calculation of phase diagrams, Academic Press, New York 1970. ΔG_{latt} is referred to here as 'lattice stability'; the values of ΔG_{latt} in fig. 5 for pure Cu, Cr, Mo, W and Co in the various crystal lattices are derived from this.

Fig. 5. *a)* The contribution ΔG_{latt} to the energy of formation as a function of the mole fraction x for the systems Cu-Cr, Cu-Mo and Cu-W. A linear relation is assumed between the points at $x = 0$ and $x = 1$. The horizontally hatched regions at the top of the figure represent the two-phase composition ranges we found experimentally. These ranges separate broad metastable single-phase ranges with the fcc and bcc structures. The single-phase ranges were found after quenching from the vapour phase. The location of the two-phase ranges corresponds reasonably well to the intersection point of the $(\Delta G_{latt}, x)$ lines. *b)* The same, for the system Co-Cu, in which cobalt has the hcp structure.

considered. Pure chromium, molybdenum and tungsten always have a body-centred cubic structure in their stable modification; see fig. 5. In these three metals, however, the fcc structure is unstable. Pure copper does have a stable fcc structure, but the bcc structure is unstable. In agreement with this, the ΔG_{latt} of the bcc structure in copper is 6 kJ/mol higher than for the fcc structure. In chromium, molybdenum and tungsten, on the other hand, the ΔG_{latt} of the bcc structure is lower than that of the fcc structure.

We have assumed that the ΔG_{latt} of the metals investigated is a linear function of the mole fraction. If we therefore draw lines connecting the points for the ΔG_{latt} of the pure metals, we find that the intersection points of the $(\Delta G_{latt}, x)$ lines for Cu with Cr, Mo or W, and for Co with Cu, agree reasonably well with the locations of the two-phase regions that we found.

Predicting amorphous phases from the phase diagram

The phase diagrams of many combinations of two metals, or of metals with metalloids, are known and available in handbooks. This is not so for diagrams in which the Gibbs free energy G is plotted as a function of the mole fraction x, at least not for all the crystalline and amorphous phases that can occur in a particular combination. This means that prediction of metastable phases from the (G, x) diagram usually requires calculation of the Gibbs free energy for different fractions and phases. The method is therefore fairly laborious.

Our method, in which direct use is made of the phase diagram, is much less laborious since it requires no calculations. *Fig. 6* shows how the method is used for predicting an amorphous phase for the nickel-zirconium combination in fig. 4. Since at a high quenching rate there is little likelihood of compounds (usually with a complicated crystal structure) being formed, we ignore the central part of the phase diagram. This leaves us mainly with the two-phase regions of the virtually pure elements with liquid, and with the liquid phase L between them. The liquidus curves are then extrapolated. If the extrapolated curves do not intersect at a temperature above room temperature, they form the limits for a composition range in which a metastable equilibrium of the liquid or the amorphous phase can exist. We thus find a composition range for the amorphous phase for Ni-Zr at room temperature that corresponds reasonably well with the ranges in fig. 4c.

For the actual formation of an amorphous phase the rate of cooling from the liquid phase must be higher than a certain critical quenching rate. For a given composition the critical quenching rate increases with
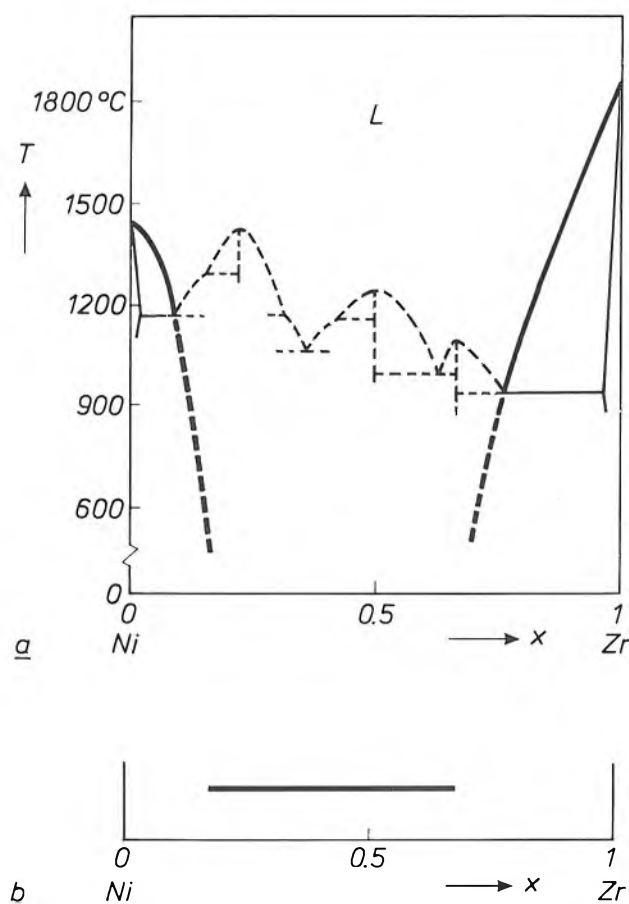
Fig. 6. The phase diagram can be used to determine the mole fractions at which an amorphous phase would be expected after quenching, in this case for the system Ni-Zr (see also fig. 4). *a*) The central part of the phase diagram is not considered because, in general, no compounds will be formed during quenching. The liquidus curves of the almost pure elements are extrapolated to room temperature. *b*) The composition range in which an amorphous phase can be expected; the range is bounded by the extrapolated curves.

the difference between the solidification temperature of the crystalline phase and the glass temperature of the amorphous phase. The glass temperature is the temperature at which the viscosity of the undercooled liquid produced by the quenching has increased to such an extent that it can be said to be an amorphous solid. In quenching from the liquid phase with a rotating wheel a quenching rate is reached that is 10^9 K/s at the most. In deposition from the vapour phase on to a substrate that is kept at room temperature, a quenching rate of about 10^{12} K/s can be calculated from energy considerations. The method used by Scott (see fig. 4c) was probably quenching of molten metal between rollers; the quenching rate that can be reached in this method is not so high, about 10^7 K/s. This explains why Buschow did find amorphous material at the fraction $x = 0.5$, where the solidification temperature of the compound NiZr is high, whereas Scott did not. At $x = 0.22$, where the compound Ni_7Zr_2 has an even higher solidification temperature, both Buschow
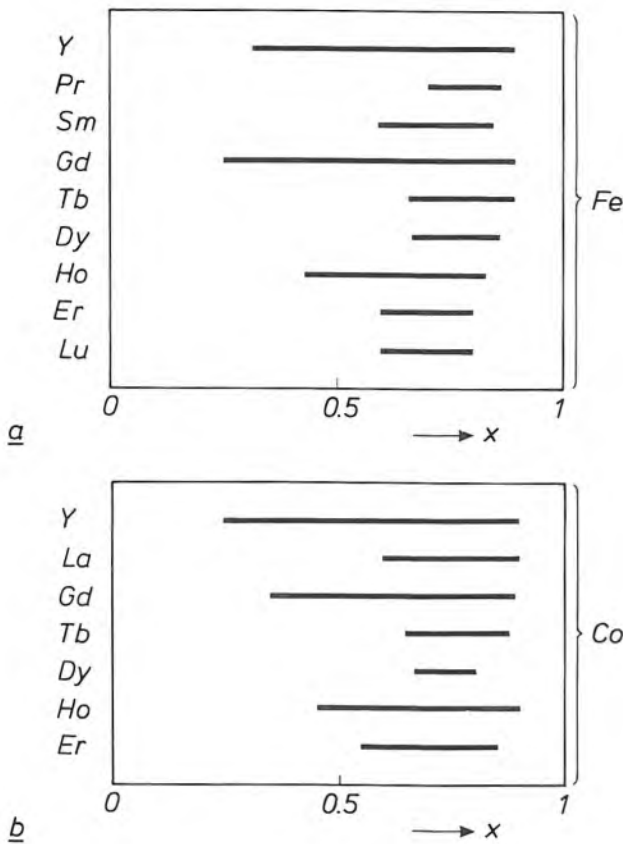
Fig. 7. Composition ranges in which amorphous material was found on quenching from the vapour phase a) for the combination of iron with yttrium and rare earths, b) for cobalt with yttrium and rare earths[2].
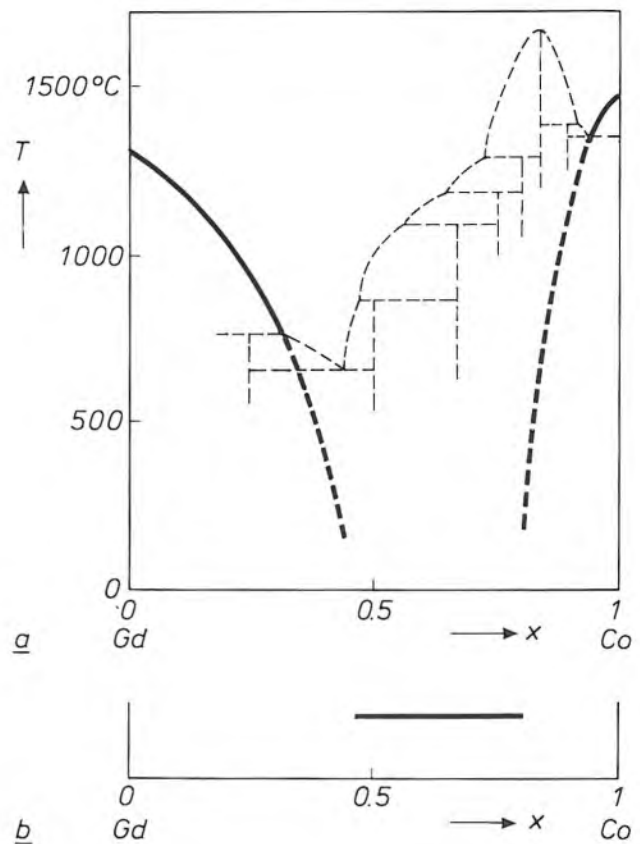
Fig. 8. Prediction of the composition range of an amorphous phase for the system gadolinium-cobalt; see also figs 6 and 7. a) Extrapolation of the liquidus curves in the phase diagram. b) The range thus found.

and Scott failed to find amorphous material. Presumably they would have done so if they had used the method of deposition from the vapour phase.

In research aimed at finding suitable ferrimagnetic materials for magneto-optical recording, many combinations of elements have been investigated at our Laboratories for the occurrence of amorphous phases [2]. The results of this work by J. W. M. Biesterbos and A. G. Dirks are presented in *fig. 7a* and *b*. They relate to combinations of iron and cobalt with yttrium and rare earths. The amorphous films were produced from the vapour phase. The advantage of this kind of amorphous material for magneto-optical recording is that the magnetic-compensation temperature can be accurately adjusted by varying the composition in a wide range. If we started from crystalline material of the combinations mentioned above, which can form compounds, we would be confined to fairly narrow composition limits corresponding to the phase diagram.

The usefulness of our method for predicting an amorphous phase is illustrated for gadolinium and cobalt in *fig. 8*. The result agrees reasonably well with the experimentally determined range in fig. 7b. The

other ranges in fig. 7 can also be predicted with phase diagrams, though not so accurately.

Amorphous (metastable) phases are known for most combinations of zirconium with 3d transition metals, e.g. nickel and zirconium; see fig. 4. It did not prove possible, however, to produce amorphous chromium-zirconium. *Fig. 9* shows that this can also be explained from the phase diagram. In Cr-Zr, unlike Ni-Zr (see fig. 6) there is no question at all of a range with a metastable liquid phase that extends to low temperatures: the extrapolated liquidus curves intersect each other at a point at about 1000 °C — far above room temperature.

The transition from stable thermodynamic equilibrium to a metastable equilibrium

When the substrate is not kept at room temperature during deposition from the vapour phase, but at a higher temperature, the term quenching is not so appropriate. In this situation transitional states can occur between the stable thermodynamic equilibrium and a metastable equilibrium. The effect of the substrate temperature T_s has been investigated by
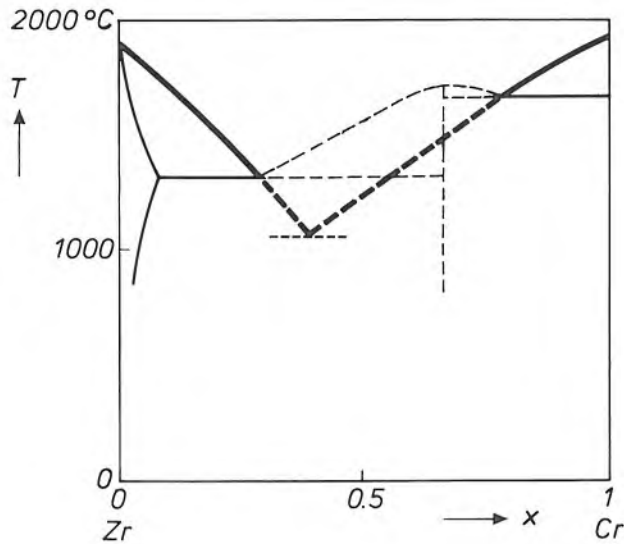
Fig. 9. The extrapolation of the liquidus curves in the phase diagram of the system zirconium-chromium. It can be seen from this that it is almost impossible to obtain amorphous Zr-Cr by quenching, since the intersection point of the extrapolated curves is at about 1000 °C.

H. T. G. Hentzell *et al.* for the system aluminium-nickel in the range $0.4 < x_{Ni} < 1$ [15]. The complicated phase diagram for this system can be seen in *fig. 10a.* The phases found by Hentzell *et al.* as a function of the substrate temperature are shown in fig. 10b. The intersection point of the curves at 300 K is the result of our own work, involving vapour deposition on an unheated substrate for varying nickel content and investigation of the structures by X-ray diffraction and transmission electron microscopy.

At $T_s > 700$ K the results of Hentzell *et al.* agree reasonably well with the phase diagram. At $300 \text{ K} < T_s < 700$ K the mobility of the atoms is on the one hand too low for a stable equilibrium to be reached, but on the other hand too high for a metastable equilibrium to be 'frozen in'. In this transitional region the phase relations are determined by a combination of atomic mobility and the tendency of the system to seek a minimum Gibbs free energy. This can lead to unexpected situations, because the three-phase region $\beta' + \alpha' + fcc$ in fig. 10b could not exist in a binary system in thermodynamic equilibrium.

At $T_s < 300$ K the α' phase is not present, possibly because the mobility of the atoms is insufficient for this phase to occur. There are then only two broad single-phase regions: that of the fcc structure of pure nickel and that of the β' structure, which corresponds to the (cubic) structure of caesium chloride. The mole fraction that corresponds to the boundary of the two single-phase regions is in agreement with the location of the intersection point of the $(\Delta G, x)$ curves for the fcc and β' structures; see fig. 10c. We do not need to
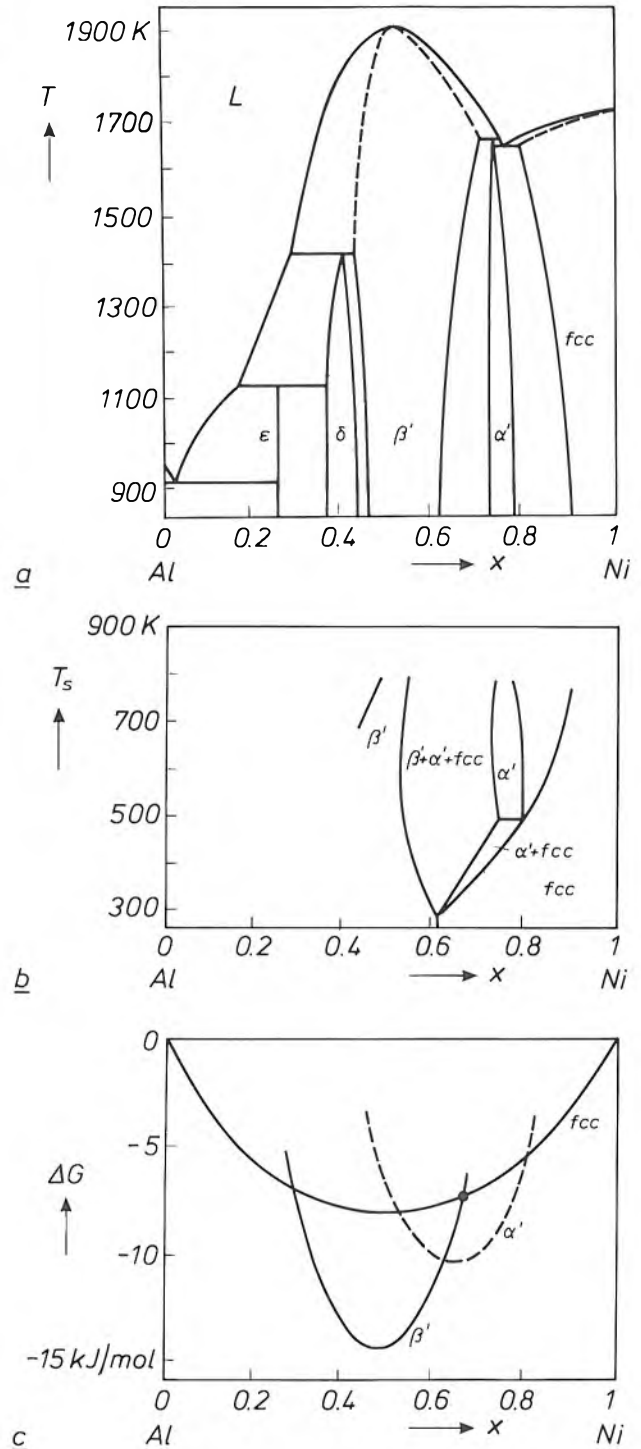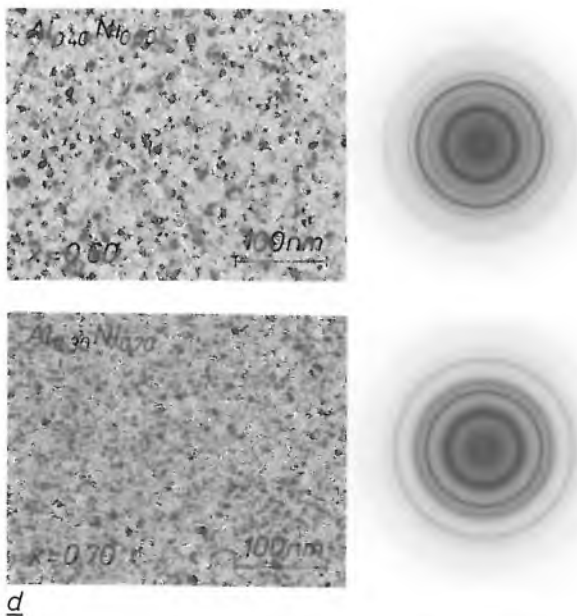

Fig. 10. The effect of the substrate temperature T_s in quenching from the vapour phase for the system aluminium-nickel. *a)* The phase diagram. ε, δ, β', α' and *fcc* crystal structures. *b)* The phase relationships as a function of the substrate temperature [15]. (The intersection point of the lines at room temperature is the result of our own research.) If T_s is equal to room temperature, there are two single-phase regions. *c)* The energy of formation ΔG as a function of x for the structures β', α' and *fcc* at room temperature. The structure α' is not formed at room temperature because it is too complicated; the corresponding curve is therefore shown dashed. The intersection point shown corresponds to the boundary of two single-phase regions on quenching. This agrees well with the results in *(b)*. *d) Left*: bright-field micrographs, *right*: electron-diffraction patterns, made with a Philips transmission electron microscope at two different mole fractions x of the $Al_{1-x}Ni_x$ film deposited from the vapour phase. The diffraction patterns are clearly different.

_d_

The results in fig. 10 demonstrate that, when the substrate temperature changes during the deposition of thin metal-alloy films from the vapour phase, there are three separate temperature regions:

• a region at high substrate temperature, where the location of the phases corresponds reasonably well to the phase diagram;

• a region at low substrate temperature, where the boundary of wide and largely metastable single-phase regions corresponds to the intersection point of the relevant $(\Delta G, x)$ curves, and

• a region at intermediate temperatures with fairly complicated phase relationships, since on the one hand the system tends towards a stable thermodynamic equilibrium and on the other hand the mobility of the atoms is limited.

consider the curve for the phase α', since this phase, as noted, is not formed at room temperature.

The boundary of the single-phase regions also follows from the micrographs in fig. 10d of structures with $x = 0.60$ and 0.70; these micrographs were made with a Philips transmission electron microscope. The bright-field pictures show an almost identical grain structure, consisting of extremely fine crystallites. The electron-diffraction patterns reveal that there has been a definite change in the crystal structure.

[15] H. T. G. Hentzell, B. Andersson and S.-E. Karlsson, Grain size and growth of Ni-rich Ni-Al alloy films, Acta Metall. 31, 2103-2111, 1983.

Summary. There is a growing interest in amorphous phases, for one reason because of the application of thin films of amorphous metal in magneto-optical recording. The phase diagram, which applies for a state of stable thermodynamic equilibrium, can often be used to predict whether an amorphous phase — invariably metastable — will occur in a binary system. This is so, for example, in combinations of iron or cobalt with rare earths, from which amorphous films have been deposited from the vapour phase to see whether they can be used as a medium for magneto-optical recording. The occurrence of metastable phases — either amorphous or crystalline — can also be predicted from the (G, x) diagram, in which no account need be taken of the (G, x) curves of phases that cannot occur owing to limited atomic mobility. The phase that does form on quenching is the one that has the lowest Gibbs free energy G at a given composition. If the substrate is kept at a higher temperature than room temperature during deposition from the vapour phase, fairly complicated phase relationships arise in a transitional region between a state of stable thermodynamic equilibrium at high temperature and a region of metastable equilibrium at room temperature.

Scientific publications

These publications are contributed by staff from the laboratories and other establishments that form part of or are assiociated with the Philips group of companies. Many of the articles originate from the research laboratories named below. The publications are listed alphabetically by journal title.

Philips GmbH Forschungslaboratorium Aachen,   *A*
  Weißhausstraße, 5100 Aachen, Germany

Philips Research Laboratory, Brussels,   *B*
  2 avenue Van Becelaere, 1170 Brussels, Belgium

Philips Natuurkundig Laboratorium,   *E*
  Postbus 80000, 5600 JA Eindhoven, The Netherlands

Philips GmbH Forschungslaboratorium Hamburg,   *H*
  Vogt-Kölln-Straße 30, 2000 Hamburg 54, Germany

Laboratoires d'Electronique et de Physique Appliquée,   *L*
  3 avenue Descartes, 94450 Limeil-Brévannes, France

Philips Laboratories, N.A.P.C.,   *N*
  345 Scarborough Road, Briarcliff Manor, N.Y. 10510, U.S.A.

Philips Research Laboratories,   *R*
  Cross Oak Lane, Redhill, Surrey RH1 5HA, England

Philips Research Laboratories, Sunnyvale,   *S*
  P.O. Box 9052, Sunnyvale, CA 94086, U.S.A.

B. Post & J. Ladell	*N*	The phases of forbidden reflections	Acta Crystallogr. **A43**	173-179	1987
O. Boser	*N*	Electromechanical resonances in ceramic capacitors and evaluation of the piezoelectric materials' properties	Adv. Ceram. Mater. **2**	167-172	1987
P. van der Putte, D. K. Sadana, E. K. Broadbent & A. E. Morgan	*S*	Growth of selective tungsten films on self-aligned $CoSi_2$ by low pressure chemical vapor deposition	Appl. Phys. Lett. **49**	1723-1725	1986
A. E. Morgan & P. Maillot	*S*	Depth profiling of As at the SiO_2/Si interface using secondary ion mass spectrometry	Appl. Phys. Lett. **50**	959-961	1987
J. Petruzzello, D. Olego, S. K. Ghandhi*, N. R. Taskar* & I. Bhat* (*Rensselaer Polytech. Inst., Troy, NY*)	*N*	Transmission electron microscopy of (001) CdTe on (001) GaAs grown by metalorganic chemical vapor deposition	Appl. Phys. Lett. **50**	1423-1425	1987
K. Mohammed, D. J. Olego, P. Newbury, D. A. Cammack, R. Dalby & H. Cornelissen	*N*	Quantum confinement and strain effects in ZnSe-Zn_xSe_{1-x} strained-layer superlattices	Appl. Phys. Lett. **50**	1820-1822	1987
A. J. Fox	*R*	Thermal design for germanium acoustooptic modulators	Appl. Opt. **26**	872-884	1987
P. J. Kelly, R. Car (*Int. School Adv. Studies, Trieste*) & S. T. Pantelides (*IBM T. J. Watson Res. Center, Yorktown Heights, NY*)	*E*	Theoretical determination of the vacancy migration energy in silicon	Defects in Semiconductors, H. J. von Bardeleben (ed.), Mater. Sci. Forum, Vol. 10-12, Trans Tech, Aedermannsdorf	115-120	1986
P. Boivin*, J. Rabier*, H. Garem* (*Lab. Métallurgie Phys., C.N.R.S., Poitiers*) & M. Duseaux	*L*	Dislocation substructures and plasticity of GaAs below 400 °C as a function of doping	Defects in Semiconductors, H. J. von Bardeleben (ed.), Mater. Sci. Forum, Vol. 10-12, Trans Tech, Aedermannsdorf	781-786	1986
S. Makram-Ebeid & P. Boher	*L*	Electron hopping between bombardment induced defects in gallium arsenide	Defects in Semiconductors, H. J. von Bardeleben (ed.), Mater. Sci. Forum, Vol. 10-12, Trans Tech, Aedermannsdorf	1075-1080	1986
E. Dupont-Nivet, J. N. Patillon, J. P. André & G. M. Martin	*L*	Study of deep levels in $Al_yGa_xIn_{1-x}P$ material grown by MOVPE	Defects in Semiconductors, H. J. von Bardeleben (ed.), Mater. Sci. Forum, Vol. 10-12, Trans Tech, Aedermannsdorf	1207-1212	1986

J. K. Chamberlain*, F. M. Clayton* (*Hirst Res. Centre, Wembley), H. Sari, P. Vandamme (CNET, Lannion) L	Receiver techniques for microwave digital radio	IEEE Commun. Mag. 24 (No. 11)	43-54	1986
J. R. Brandsma, A. A. M. L. Bruekers & J. L. W. Kessels E	PHILAN: a fiber-optic ring for voice and data	IEEE Commun. Mag. 24 (No. 12)	16-22	1986
J. Khurgin N	Theoretical and experimental investigation of amplified spontaneous emission in electron-beam-pumped semiconductor lasers	IEEE J. QE-23	194-204	1987
G. R. Gao N	Maximum pipelining linear recurrence on static data flow computers	Int. J. Parallel Program. **15**	127-149	1986
A. J. M. Houtsma (Inst. Perception Res., Eindhoven) & T. D. Rossing (Northern Illinois Univ., DeKalb, IL)	Effects of signal envelope on the pitch of short complex tones	J. Acoust. Soc. Am. **81**	439-444	1987
T. Baller*, D. J. Oostra*, A. E. de Vries* (*FOM, Amsterdam) & G. N. A. van Veen E	Laser-induced etching of Si with chlorine	J. Appl. Phys. **60**	2321-2326	1986
A. H. van Ommen E	Diffusion of ion-implanted Sb in SiO_2	J. Appl. Phys. **61**	993-997	1987
J. J. Harris, C. T. Foxon, K. W. J. Barnham, D. E. Lacklison, J. Hewett & C. White R	Two-dimensional electron gas structures with mobilities in excess of $3 \times 10^6 cm^2 V^{-1} s^{-1}$	J. Appl. Phys. **61**	1219-1221	1987
J. M. Towner & B. Coulman S	Effects of vanadium and chromium on aluminum electromigration	J. Appl. Phys. **61**	1392-1403	1987
N. D. Young, J. B. Clegg & E. A. Maydell-Ondrusz (Univ. Surrey, Guildford) R	Low-temperature annealing of shallow arsenic-implanted layers	J. Appl. Phys. **61**	2189-2194	1987
R. Bar-Gadda S	A theoretical prediction of film thickness profiles in a mixed convection-diffusion regime for the chemical vapor deposition of polysilicon in annular tubes	J. Electrochem. Soc. **133**	2123-2131	1986
A. E. Morgan, E. K. Broadbent, M. Delfino, B. Coulman & D. K. Sadana S	Characterization of a self-aligned cobalt silicide process	J. Electrochem. Soc. **134**	925-935	1987
H. H. R. Jansen (Philips Lighting Div., Eindhoven)	Aspects of the recrystallization kinetics of doped tungsten	Philips J. Res. **42**	3-14	1987
G. Dittmer & U. Niemann A	Evaluation of thermodynamic data on zirconium and hafnium halides and oxyhalides by means of transport experiments	Philips J. Res. **42**	15-40	1987
G. Dittmer & U. Niemann A	The influence of solid phases on transport cycles in halogen-filled incandescent lamps	Philips J. Res. **42**	41-57	1987
E. Fischer A	Modelling of low-power high-pressure discharge lamps	Philips J. Res. **42**	58-86	1987
J. J. de Groot*, J. Schlejen**, J. P. Woerdman** (**Univ. Leiden) & M. F. M. de Kieviet* (*Philips Lighting Div., Eindhoven)	The influence of NaNa, NaHg and NaXe molecules on the spectrum of the high-pressure sodium lamp	Philips J. Res. **42**	87-101	1987
W. van Erk* & T. Rietveld* (*Philips Lighting Div., Eindhoven)	The reaction of rare-earth metal iodides with the silica wall in metal halide discharge lamps	Philips J. Res. **42**	102-118	1987
G. de With E	Preparation, microstructure and properties of $Y_3Al_5O_{12}$ ceramics	Philips J. Res. **42**	119-130	1987
W. J. A. Goossens E	Excess free energy due to hard-core repulsions for the cholesteric and smectic phases	Phys. Rev. A **35**	1843-1846	1987
G. Duggan & H. I. Ralph R	Exciton binding energy in type-II GaAs-(Al,Ga)As quantum-well heterostructures	Phys. Rev. B **35**	4152-4154	1987
L. Knox, P. Patt & R. Maresca N	Design of a flight qualified long-life cryocooler	Proc. 3rd Cryocooler Conf. on Refrigeration for cryogenic sensors & electronic systems, Boulder, CO, 1984	1-20	1984

P. van der Putte	S	The reaction kinetics of the H_2 reduction of WF_6 in the chemical vapor deposition of tungsten films	Proc. Workshop Tungsten and other Refactory Metals for VLSI Applications, Palo Alto, CA, 1986	77-84	1987
P. van der Putte, D. K. Sadana, E. K. Broadbent & A. E. Morgan	S	Growth of selective tungsten on self-aligned $CoSi_2$ by low pressure chemical vapor deposition	Proc. Workshop Tungsten and other Refactory Metals for VLSI Applications, Palo Alto, CA, 1986	101-107	1987
E. K. Broadbent & J. M. Towner	S	Electromigration-induced short circuit failure in aluminum/tungsten (CVD) conductors	Proc. Workshop Tungsten and other Refactory Metals for VLSI Applications, Palo Alto, CA, 1986	247-255	1987
L. Gutai, M. Delfino & J. M. DeBlasi	S	Thermal stability of Al/W/p-n Si contacts during post-metallization annealing	Proc. Workshop Tungsten and other Refactory Metals for VLSI Applications, Palo Alto, CA, 1986	265-272	1987
D. R. Gentner	N	Timing of skilled motor performance: Tests of the proportional duration model	Psychol. Rev. **94**	255-276	1987
J. Reimer, A. Bhattacharyya & K. Ritz	S	Electron beam induced current analysis of voltage breakdown sites in thin MOS oxides	Scanning Microsc. **1**	23-30	1987
V. Lacroix	B	Pixel labeling in a second-order Markov mesh	Signal Process. **12**	59-82	1987
F. J. A. M. Greidanus & J. T. C. van Roosmalen	E	ODMR experiments on the 1.65eV luminescence in GaP:Cu	Solid State Commun. **61**	653-657	1987
H. C. de Graaff	E	Polycrystalline silicon in integrated circuits	Solid State Sci. **57**	170-184	1984
S. van Lerberghe	E	Digital adaptive multipath equalization of FM signals	Thesis, Brussels	1-226	1987
A. H. M. van Roermund	E	Noise and accuracy in switched capacitor modulation circuits	Thesis, Heverlee	1-250	1987

Contents of Philips Telecommunication and Data Systems Review **45**, No. 2, 1987

J. R. Gray: MAESTRO: science in the art of software production (pp. 1-9)

J. F. Briend & J. J. Plancke: French PTT MINITEL and LECAM programme (pp. 10-26)

B. Jurgens: MPX operating system (pp. 27-44)

L. T. van der Bijl & P. H. A. Timmers: The application environment of the P9X00 (pp. 45-60)

Contents of Electronic Components & Applications **8**, No. 2, 1987

R. Croes & A. de Pagter: ACL . . . Advanced CMOS Logic that lengthens the stride of low-power systems (pp. 66-75)

S. Baliga, G. Goodhue & J. Jenkins: Microcontroller eases I/0 processing burden (pp. 76-80)

D. Haslam & M. J. Hill: Breakover diodes for the protection of telephone equipment (pp. 81-86)

F. A. Pieters: Quality — dry reed switches (pp. 87-94)

G. Conn: The SCC68070 — a monolithic 68000 CPU and peripherals (pp. 95-100)

T. v.d. Wouw: Cascode-driven SMPS with high-voltage darlington transistors (pp. 101-108)

N. Siddique & F. Krupecki: Fast controller converts large static RAMs to FIFO buffers (pp. 109-112)

S. Baliga: Managing graphics displays using a microcontroller (pp. 113-117)

D. Eckstein & R. W. Stamer: Improved varicaps for tv tuners (pp. 118-124)

The CM12/STEM electron microscope has a Twin objective and microprocessor control. With this special objective it is possible to switch over quickly from a conventional TEM mode, with a direct image of the specimen or diffraction pattern on a fluorescent screen in the projection chamber, to a STEM mode, where the specimen is scanned by the illuminating beam and a detector signal is converted into a video signal for one of the monitors. Because of the special magnetic configuration of the objective, which includes a mini-condenser lens, this switch-over produces hardly any change in the heat-flow conditions in and around the polepieces. The CM12/STEM is very much easier to operate than other microscopes because the microprocessor guides the user to the various operating modes and features by providing information on a control screen. The use of 'soft-keys' and multi-functional controls on the panels keeps the number of manual controls relatively small. Micrographs demonstrate the resolution and some of the many features of the instrument.

Fluctuations in the optical power of semiconductor lasers can arise because of radiation returning to the laser cavity after reflection from a surface outside the cavity. These fluctuations are undesirable in many applications in which information is optically transmitted as variations in laser power. Experiments and calculations have been carried out to gain a better understanding of the ways in which these fluctuations are affected by the various laser parameters. Experimental and theoretical results agree well. Conditions can now be indicated in which there is very little variation in laser power as a result of feedback of optical power.

There is a growing interest in amorphous phases, for one reason because of the application of thin films of amorphous metal in magneto-optical recording. The phase diagram, which applies for a state of stable thermodynamic equilibrium, can often be used to predict whether an amorphous phase — invariably metastable — will occur in a binary system. This is so, for example, in combinations of iron or cobalt with rare earths, from which amorphous films have been deposited from the vapour phase to see whether they can be used as a medium for magneto-optical recording. The occurrence of metastable phases — either amorphous or crystalline — can also be predicted from the (G,x) diagram, in which no account need be taken of the (G,x) curves of phases that cannot occur owing to limited atomic mobility. The phase that does form on quenching is the one that has the lowest Gibbs free energy G at a given composition. If the substrate is kept at a higher temperature than room temperature during deposition from the vapour phase, fairly complicated phase relationships arise in a transitional region between a state of stable thermodynamic equilibrium at high temperature and a region of metastable equilibrium at room temperature.

I wish to subscribe to

PHILIPS TECHNICAL REVIEW

(date)   (signature)

Please tick the appropriate box

Regular subscription   80 guilders or U.S. $ 35.00 per volume   ☐

> The subscription includes postage and will start with Vol. 43, No. 1.
> Please pay when you receive our invoice.

Student's subscription   32 guilders or U.S. $ 14.00 per volume   ☐

> Please send a copy of your student's card or other written proof that you are a student;
> valid for two volumes.

Name

Initials

Title

Address

Administration Department
Philips Technical Review

Philips Research Laboratories
Building WY 136

P.O. Box 80 000

5600 JA   Eindhoven
**   The Netherlands**

OTHER PHILIPS PUBLICATIONS

Philips Journal of Research

A publication in English on the research work carried out in the various Philips laboratories. Published in annual volumes of six issues each of about 100 pages, size 15½ × 23½ cm.

Philips Telecommunication and Data Systems Review

A publication in English on systems and equipment for business communications, computer systems and networks, telecommunication services, radio communications and dictation. Published in volumes of four issues, about 40 pages per issue, size 21½ × 29½ cm.

Electronic Components and Applications

A publication in English, containing articles dealing with the theory and practice of electronic components and materials. Four issues per year, about 60 pages per issue, size 21 × 29½ cm.

Medicamundi

A publication in English on radiology, nuclear medicine and medical electronics. Three issues per volume, about 60 pages per issue, size 21 × 29½ cm.

Forthcoming issues of Philips Technical Review will include articles on:

CARIN

The oxide film in MOS devices

Optical multiplexers and demultiplexers

An integrated digital signal processor

Contents

Page

PHILIPS